



# LUND UNIVERSITY

## Lineshape in Quantum Cascade Lasers - Temperature, Screening and Broadening

Nelander, Rikard

2009

[Link to publication](#)

*Citation for published version (APA):*

Nelander, R. (2009). *Lineshape in Quantum Cascade Lasers - Temperature, Screening and Broadening*. [Doctoral Thesis (compilation), Mathematical Physics].

*Total number of authors:*

1

### General rights

Unless other specific re-use rights are stated the following general rights apply:

Copyright and moral rights for the publications made accessible in the public portal are retained by the authors and/or other copyright owners and it is a condition of accessing publications that users recognise and abide by the legal requirements associated with these rights.

- Users may download and print one copy of any publication from the public portal for the purpose of private study or research.
- You may not further distribute the material or use it for any profit-making activity or commercial gain
- You may freely distribute the URL identifying the publication in the public portal

Read more about Creative commons licenses: <https://creativecommons.org/licenses/>

### Take down policy

If you believe that this document breaches copyright please contact us providing details, and we will remove access to the work immediately and investigate your claim.

LUND UNIVERSITY

PO Box 117  
221 00 Lund  
+46 46-222 00 00

LINESHAPE IN QUANTUM CASCADE LASERS  
— TEMPERATURE, SCREENING AND  
BROADENING

RIKARD NELANDER



DIVISION OF MATHEMATICAL PHYSICS  
FACULTY OF SCIENCE  
LUND UNIVERSITY 2009

©2009 Rikard Nelander

Paper I ©2007 by American Institute of Physics.

Paper II ©2008 by American Institute of Physics.

Paper III ©2009 by WILEY-VCH Verlag GmbH & Co. KGaA, Weinheim.

Paper IV ©2009 by Society of Photo-Optical Instrumentation Engineers (SPIE)  
and the authors.

Paper V ©2009 by American Institute of Physics.

Printed in Sweden November 2009 at Tryckeriet i E-huset, Lund.

ISBN-978-91-628-7956-3

LINESHAPE IS QUANTUM CASCADE LASERS  
— TEMPERATURE, SCREENING AND  
BROADENING

RIKARD NELANDER

DIVISION OF MATHEMATICAL PHYSICS

FACULTY OF SCIENCE

LUND UNIVERSITY, SWEDEN

DISSERTATION FOR THE DEGREE OF  
DOCTOR OF PHILOSOPHY IN ENGINEERING

THESIS ADVISOR: PROF. ANDREAS WACKER


FACULTY OPPONENT: PROF. GERALD BASTARD, LPA-ENS, PARIS

ACADEMIC DISSERTATION WHICH, BY DUE PERMISSION OF THE FACULTY OF SCIENCE AT LUND  
UNIVERSITY, WILL BE PUBLICLY DEFENDED ON FRIDAY, DECEMBER 4, 2009, AT 14:00 IN  
LECTURE HALL B, SÖLVEGATAN 14A, LUND, FOR THE DEGREE OF DOCTOR OF PHILOSOPHY  
IN ENGINEERING.

Organization LUND UNIVERSITY Department of Physics Division of Mathematical Physics, Faculty of Science Box 118 SE-22100 LUND, SWEDEN		Document name DOCTORAL DISSERTATION	
		Date of issue 9 November 2009	
Author(s) Rikard Nelander		Sponsoring organization	
Title and subtitle Lineshape in Quantum Cascade Lasers - Temperature, Screening and Broadening			
Abstract <p>This dissertation deals with the optical properties of Quantum Cascade Lasers (QCLs). Studies are performed using transport calculations employing the theory of Non-Equilibrium Green's Functions, and screening is studied within the Random Phase Approximation. Focus is put on the temperature dependent effects in THz QCLs.</p> <p>After a popular science summary and a presentation and discussion of the theory and the methods used in this work, five original papers are presented.</p> <p>Paper I investigates the evolution of the optical spectra as a function of bias for a mid-infrared QCL. It is found that most spectral features can be explained by a shift of the electrons from the active region to the injection region of the laser.</p> <p>Paper II investigates the gain spectra of a THz QCL for increasing temperature. It is found that increased broadening, with constant population inversion, decrease the peak gain at low temperatures. The increased broadening is addressed to enhanced scattering due to reduced screening at elevated temperatures.</p> <p>Paper III investigates the impact of acoustic phonon scattering on the gain spectra for THz QCLs. It is found that at the temperatures of interest, acoustic phonon scattering has a marginal effect on the gain properties of THz QCLs.</p> <p>In Paper IV different aspects of the gain spectra are summarized with focus on the theoretical description using Non-Equilibrium Green's Functions and density matrix theory. Here, the focus lies on dispersive gain and correlations effects.</p> <p>Paper V investigates how the subband structure and the different subband temperatures affect screening. It is found that screening has a strong impact on scattering for increasing temperature, and that isotropic Debye screening is an excellent approximation for THz QCLs at temperatures of interest.</p>			
Key words Quantum Cascade Lasers, quantum wells, spectral lineshape, Non-Equilibrium Green's Functions, screening, temperature dependence			
Classification system and/or index terms (if any)			
Supplementary bibliographical information		Language English	
ISSN and key title		ISBN 978-91-628-7956-3	
Recipient's notes		Number of pages 130	Price
		Security classification	

Distribution by (name and address) Rikard Nelander, Div. of Math. Phys., LU, Box 118, SE-22100 LUND

I, the undersigned, being the copyright owner of the abstract of the above-mentioned dissertation, hereby grant to all reference sources permission to publish and disseminate the abstract of the above-mentioned dissertation.

Signature 

Date 3 November 2009

This thesis is based on the following publications:

- I R. Nelander, A. Wacker, M. F. Pereira Jr.,  
D. G. Revin, M. R. Soulby, L. R. Wilson, J. W. Cockburn,  
A. B. Krysa, J. S. Roberts, and R. J. Airey  
**Fingerprints of spatial charge transfer  
in quantum cascade lasers**  
*Journal of Applied Physics* **102** 113104 (2007).  
©2007 American Institute of Physics. Reprinted with permission.
- II Rikard Nelander and Andreas Wacker  
**Temperature dependence of the gain profile  
for terahertz quantum cascade lasers**  
*Applied Physics Letters* **92** 081102 (2008).  
©2008 American Institute of Physics. Reprinted with permission.
- III Rikard Nelander and Andreas Wacker  
**Temperature degradation of the gain transition  
in terahertz quantum cascade lasers  
– the role of acoustic phonon scattering**  
*Physica Status Solidi (c)* **6** 579 (2009)  
©2009 WILEY-VCH Verlag GmbH & Co. KGaA, Weinheim.  
Reprinted with permission.
- IV Andreas Wacker, Rikard Nelander, and Carsten Weber  
**Simulation of gain in quantum cascade lasers**  
*Proceedings of SPIE* **7230** 72301A-1 (2009)  
©2009 SPIE and the authors.
- V Rikard Nelander and Andreas Wacker  
**Temperature dependence and screening models  
in quantum cascade structures**  
*Journal of Applied Physics* **106** 063115 (2009).  
©2009 American Institute of Physics. Reprinted with permission.

Publications not included in this thesis due to overlapping content:

- VI M. F. Pereira, Jr., R. Nelander, A. Wacker, D. Revin,  
J. Cockburn, M. Soulby, L. Wilson, A. Krysa, J. Roberts,  
and R. Airey  
**Characterization of Intersubband Devices Combining a  
Nonequilibrium Many Body Theory with Transmission  
Spectroscopy Experiment**  
*Journal of Materials Science: Material in Electronics*  
**18** 689 (2007).
  
- VII D. G. Revin, M. R. Soulby, J. W. Cockburn, A. B. Krysa,  
J. S. Roberts, R. J. Airey, R. Nelander, M. F. Pereira,  
and A. Wacker  
**Probing the electronic and optical properties of  
quantum cascade lasers under operating conditions**  
*Optical Methods in the Life Sciences* **6386** U83 (2006).

# Contents

<b>A</b>	<b>Introduction, Motivation, and Methods</b>	<b>1</b>
1	Popular Science Summary	3
2	Populärvetenskaplig sammanfattning	5
3	The Quantum Cascade Laser	7
3.1	Principle of Operation . . . . .	8
3.2	Current Status . . . . .	10
4	Heterostructures	13
4.1	Heterostructures – Quantum Wells . . . . .	14
4.2	Periodic Structures – Superlattices . . . . .	15
5	Scattering Mechanisms	19
5.1	Phonon Scattering . . . . .	19
5.2	Impurity Scattering . . . . .	22
5.3	Interface Roughness Scattering . . . . .	22
5.4	Alloy Scattering . . . . .	24
5.5	Electron-Electron Scattering . . . . .	25
6	Transport Models	27
6.1	Rate Equations . . . . .	27
6.2	Monte Carlo Method . . . . .	28
6.3	Density Matrix Theory . . . . .	29
6.4	Non-Equilibrium Green’s Functions . . . . .	29
6.5	Scattering Averaging . . . . .	31
6.6	Summary . . . . .	32
7	Screening	33
7.1	Induced Charge in Quantum Wells . . . . .	33
7.2	Isotropic Screening . . . . .	35



7.3	Screened Electron-Electron Interaction . . . . .	36
<b>8</b>	<b>Light Matter Interaction</b>	<b>41</b>
8.1	Microscopic Approach . . . . .	43
8.2	$\vec{p} \cdot \vec{A}$ vs. $\vec{r} \cdot \vec{E}$ . . . . .	44
8.3	Spectral Broadening and Correlation Effects . . . . .	47
8.4	Dispersive Gain . . . . .	48
8.5	Spatially Resolved Gain . . . . .	50
<b>9</b>	<b>Temperature in THz Lasers</b>	<b>51</b>
9.1	Thermal Backfilling . . . . .	52
9.2	Thermally Activated Phonon Emission . . . . .	53
9.3	Spectral Broadening and Temperature Dependence of Screening	55
9.4	Broadening and Resonant Injection . . . . .	55
<b>10</b>	<b>Summary and Outlook</b>	<b>57</b>
	<b>Appendices</b>	<b>61</b>
<b>A</b>	<b>Polarization Function</b>	<b>61</b>
<b>B</b>	<b>Coulomb Interaction Matrix Elements</b>	<b>65</b>
	<b>References</b>	<b>68</b>
	<b>Acknowledgments</b>	<b>75</b>
<b>B</b>	<b>The Papers</b>	<b>77</b>
	<b>The Papers — Summary</b>	<b>79</b>
<b>I</b>	<b>Fingerprints of spatial charge transfer in quantum cascade lasers</b>	
<b>II</b>	<b>Temperature dependence of the gain profile for terahertz quantum cascade lasers</b>	
<b>III</b>	<b>Temperature degradation of the gain transition in terahertz quantum cascade lasers – the role of acoustic phonon scattering</b>	

**IV Simulation of gain in quantum cascade lasers**

**V Temperature dependence and screening models in quantum cascade structures**



## Part A

# Introduction, Motivation, and Methods



# 1

## Popular Science Summary

Many of the mass produced commodity products we encounter in our every day life, such as laser printers, laser pointers, CD and DVD players contain diode lasers. Also, telephone communication and Internet nowadays rely on fiber optics communication technology for data transfer, in which diode lasers are used as light source. Most of these devices emit light with wavelengths in, or close to, the visible range. However, in certain situations this is a limitation. For instance, most gases have clear absorption features in the infrared region (IR) of the electromagnetic spectrum, while being invisible to the naked eye. In this spectral region, the light has longer wavelength than visible light. Therefore, a diode laser emitting light in the IR region would be useful for gas detection.

A second situation where long wavelength light is advantageous is at the security screening at airports. Terahertz (THz) radiation, sometimes called T-rays, with even longer wavelengths than IR, would penetrate clothes but not enter the body, unlike harmful X-ray radiation. This type of security screening was recently installed at Manchester Airport<sup>1</sup>. Other potential applications are dental imaging and detection of skin cancer. The quantum cascade laser, studied in this thesis, is a small and compact laser emitting in both the IR and THz region.

Both the standard diode laser and the quantum cascade laser are build from semiconductor materials. However, as the light emitted by the diode laser is determined by the so-called band gap, which is a property of the material, the wavelength of the light emitted from the quantum cascade laser is instead dependent of how the laser is designed.

Quantum cascade lasers are made by putting thin layers of two different semiconductor material on top of each other. There are typically 1000 layers in a quantum cascade laser and in some cases these layers are only a few layers of atoms thick. When the layers are connected to a battery, electrons will flow from layer to layer in a steplike manner, see Fig. 1.1.

A useful analogy is that in standard diode lasers the electrons flow like water down a water fall, and every electron emit a little bit of light in the fall.

---

<sup>1</sup>See, *e.g.*, Swedish newspaper Dagens Nyheter 13 Oct 2009, "Nakenröntgen i Manchester".

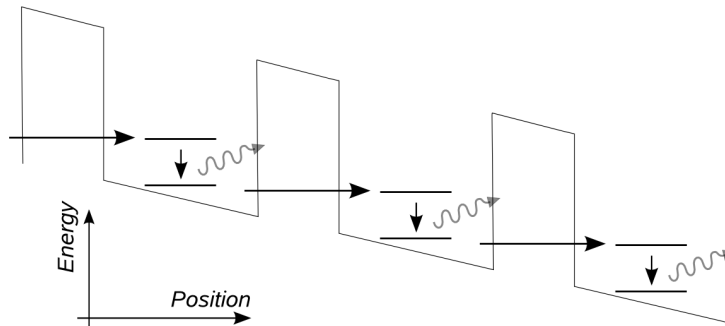


Figure 1.1: Sketch of a quantum cascade laser. The thin line is the electron potential created by the layer structure. Electrons flow, as indicated by black arrows, between discrete states (black lines). When the electrons fall down in energy light is emitted (grey arrows). The slope of the whole structure is given by an applied voltage. The structure above, where only two layers are repeated is somewhat simplified. A realistic structure can be seen on the cover of this thesis or in Fig. 3.2.

The color of the light is determined by the height of the waterfall. On the other hand, in quantum cascade lasers electrons flow like water down a staircase, and at every step light is emitted. The fundamental difference is that the height of the steps are determined by the width of the layers and not the type of semiconductor material. Also, due to the very many layers, the electrons emit light multiple times while going through the laser.

The operational principle of the quantum cascade laser was first proposed almost 40 years ago. However, it took until 1994 for the technology to produce these thin layers of high quality materials reached the stage for a working quantum cascade laser to be built. Since then, the research field of quantum cascade lasers has grown in many directions. After the first IR quantum cascade laser operating at room temperature in 2002, this type is now commercially available. The THz lasers currently operate up to  $-80^{\circ}\text{C}$ , and are therefore rarely used in applications.

This thesis focus on what mechanism affect and degrade the laser performance. More specifically, the temperature dependence screening, a consequences from the fact that electrons repel each other, is investigated. In a longer perspective, this thesis might aid the progress of the research field, such that, in future, the THz quantum cascade laser will operate at room temperature. Then, maybe, the waiting lines at airports would be shorter, the radiation exposure at the dentist would be less, and skin cancer detection would be faster and more accurate.

# 2

## Populärvetenskaplig sammanfattning

Många av de massproducerade apparater vi stöter på i vår vardag, såsom laser-skrivare, laserpekare, CD- och DVD-spelare innehåller diodlasrar. Även telefoni och Internet använder numera fiberoptik för dataöverföring där diodlasrar används som ljuskällor. De flesta av dessa lasrar avger ljus med våglängder inom strax eller utanför det synliga området. I vissa situationer är detta en begränsning. Till exempel har de flesta gaser tydliga absorptionslinjer i det infraröda (IR) området av det elektromagnetiska spektrumet, samtidigt som de är osynliga för blotta ögat. I detta spektrala område har ljuset en längre våglängd än synligt ljus. Därför skulle en diodlaser som avger ljus i IR-området vara mycket användbar för att t.ex. detektera gaser.

En annan tillämpning där ljus med lång våglängd vore fördelaktigt är vid säkerhetskontroller på flygplatser. Terahertzstrålning (THz), med ännu längre våglängder än IR, skulle tränga igenom kläder men inte komma in i kroppen till skillnad från skadlig röntgenstrålning. Denna typ av säkerhetskontroll har nyligen installerats vid Manchesters flygplats<sup>1</sup>. Andra potentiella tillämpningar är tandröntgen och diagnostisering av hudcancer. Kvantkaskadlasern, som studeras i denna avhandling, är en liten och kompakt laser som sänder ut ljus i både IR- och THz-området.

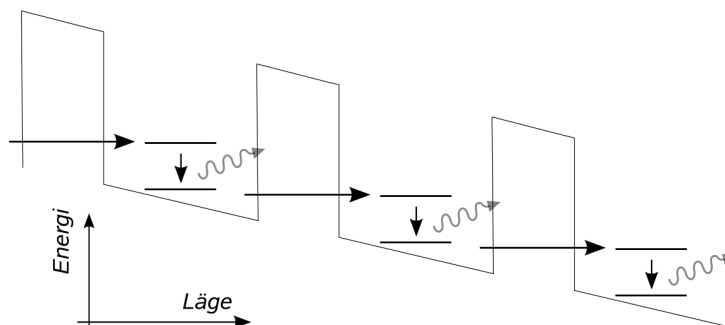
Både den vanliga diodlasern och kvantkaskadlasern är tillverkade av halvledarmaterial. Då våglängden på ljuset från diodlasern bestäms av det så kallade bandgapet, en egenskap hos materialet, så är våglängden från kvantkaskadlasern istället beroende av hur lasern är konstruerad.

Kvantkaskadlasrar tillverkas genom att tunna skikt av två olika halvledarmaterial läggs ovanpå varandra. Det finns vanligen ca 1000 lager i en kvantkaskadlaser och i vissa fall är dessa lager bara några få atomlager tjocka. När lagren ansluts till ett batteri kommer elektroner att flöda från lager till lager på ett stegliskt sätt, se figur 2.1.

---

<sup>1</sup>Se t.ex. Dagens Nyheter 13 oktober 2009, "Nakenröntgen i Manchester".





Figur 2.1: Skiss av en kvantkaskadlaser. Den tunna linjen är elektronpotentialen som skapats av lagerstrukturen. Elektronerna flödar, vilket indikeras av svarta pilar mellan olika energitillstånd (svarta linjer). När elektronerna faller nedåt i energi utsänds ljus (grå pilar). Lutningen på strukturen ges av en pålagd spänning. Strukturen ovan, där endast två lager upprepas tre gånger, är något förenklad. En realistisk struktur kan ses på omslaget till denna avhandling eller i figur 3.2.

En användbar analogi är att i en vanlig diodlaser flödar elektronerna som vatten ner för ett vattenfall och varje elektron avger lite ljus i fallet. Färgen på ljuset bestäms av höjden på vattenfallet. I kvantkaskadlasern flödar elektronerna som vatten ner för en trappa och vid varje steg utsänds ljus. Den fundamentala skillnaden är att höjden på stegen bestäms av bredden på lagren och inte av typen av halvledarmaterial. På grund av de många lagren avger elektronerna också ljus flera gånger då de passerar igenom lasern.

Principen för laserverkan i kvantkaskadlasern föreslogs för nästan 40 år sedan. Emellertid dröjde det fram till 1994 innan tekniken att tillverka dessa tunna lager av högkvalitativa material nått en fungerande nivå för att en kvantkaskadlaser kunde byggas. Sedan dess har forskningen kring dessa lasrar fortsatt i flera riktningar. Efter att den första kvantkaskadlasern i IR-området nådde rumstemperatur 2002 är nu denna typ kommersiellt tillgänglig. Kvantkaskadlasrar i THz-området fungerar för närvarande bara upp till  $-80^{\circ}\text{C}$  och är därför svåra att tillämpa praktiskt.

Denna avhandling fokuserar på de mekanismer som påverkar och försämrar laserns prestanda. Mer specifikt studeras temperatureberoendet hos skärning, en effekt av att elektroner repelerar varandra. I ett längre perspektiv kan denna avhandling stödja framsteg inom forskningsområdet så att kvantkaskadlasrar i THz-området i framtiden kan fungera vid rumstemperatur. Då skulle köer på flygplatser kunna bli kortare, strålningsexponering hos tandläkaren vara mindre och metoder för att upptäcka hudcancer skulle kunna bli snabbare och mer exakta.

# 3

## The Quantum Cascade Laser

The Quantum Cascade Laser (QCL) was first experimentally realized at Bell Labs in 1994 [1] after the theoretical study by Esaki and Tsu on negative differential conductance in superlattices in 1970 [2]. This system was also studied by Kazarinov and Suris in 1971 [3] when the authors proposed amplification of electromagnetic radiation between different subbands. This effect was explained in more details by the same authors the following year [4].

The QCL is an unipolar opto-electronic semiconductor device with laser emission now covering a large range of the electromagnetic spectrum, from the infrared (IR) to the terahertz (THz) region. These regions are important in many technological applications such as gas sensing, environmental monitoring, telecommunications and security screening [5].

The standard semiconductor diode laser is a mature technology used in a variety of applications, such as laser pointers, laser printer, DVD/CD-players etc. They are efficient, compact and cheap. However, their spectral range is limited to the band gap of the lasing material. This is due to the operational principle of these interband lasers, namely that electrons in the conduction band and holes in the valence band recombine and photons are emitted. The frequency of the light is determined by the band gap of the material. The QCL differs in a fundamental way from the ordinary diode laser. Here, the light is emitted by transitions between subbands in quantum wells formed in the conduction band.

Quantum wells are manufactured by growing thin layers of different semiconductor materials, often only a few atom layers thick, on top of each other, see right part of Fig. 3.1. A step-like conduction band potential is created, which confines the electrons in the growth direction. Electronic states are formed in these quantum wells at discrete energies. These energies are determined by the well widths and material parameters, such as effective masses, and conduction band offsets. In QCLs, inverted populations between these subbands give rise to the laser action. The main advantage is that by tailoring the dimensions of the quantum wells the energy spacing between the lasing subbands can be controlled, which determines the lasing frequency.

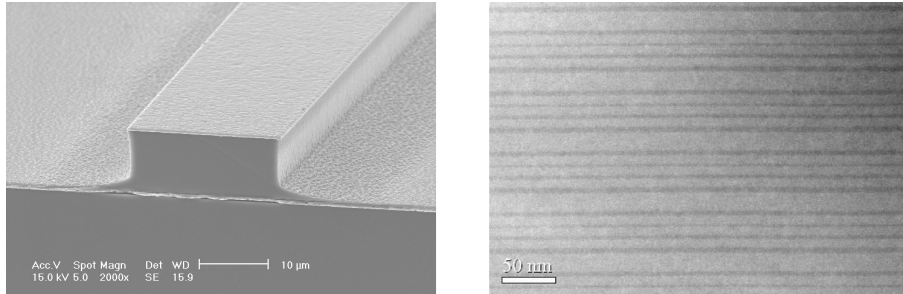


Figure 3.1: A THz Laser. *Left:* Scanning electron microscope image of a GaAs/Al<sub>0.15</sub>Ga<sub>0.85</sub>As THz QCL covered on top by a metal waveguide. The laser ridge is 25  $\mu\text{m}$  wide with a 10  $\mu\text{m}$  thick active region. For more details see Ref. [6]. *Right:* Transmission electron micrograph of five periods of semiconductor layers from the front side of the laser ridge to the left. The dark regions correspond to Al<sub>0.15</sub>Ga<sub>0.85</sub>As and the bright to GaAs. The device constitutes of approx. 200 periods, corresponding to 1600 semiconductor layers, each only a few atom layers thick. Under operation, a voltage is applied between the top and bottom of the laser ridge, which causes an electron flow governed by scattering and coherent evolution. The device studied in Papers II-V is identical to the one in the images. The potential structure is depicted on the cover of this thesis. [Courtesy of S. Kumar].

### 3.1 Principle of Operation

The operational principle of most lasers is to have more electrons in an excited state than in a state with lower energy, a situation known as population inversion. This is a highly non-equilibrium state and is often difficult to achieve and maintain. The inversion can be achieved either by optical or electrical pumping, the latter is the case for the QCL. Practically, this means that the quantum wells in QCLs are tailored such that a population inversion between two specific subbands is built up when a certain bias is applied to the device.

The two key issues to obtain a large population inversion are a long lifetime for the upper laser state and a short for the lower laser state. Efficient filling of the upper laser subband from an injector subband together with a minimum of outward transport channels is important to reach a highly populated upper laser subband.

Longitudinal optical (LO) phonons couple strongly to electrons and have an almost constant dispersion close to 36 meV in most semiconductors of interest. This scattering mechanism is used in the most common way of achieving a short lifetime in the lower laser subband. The quantum wells are tailored such that there is an ejector subband located one optical phonon energy below.

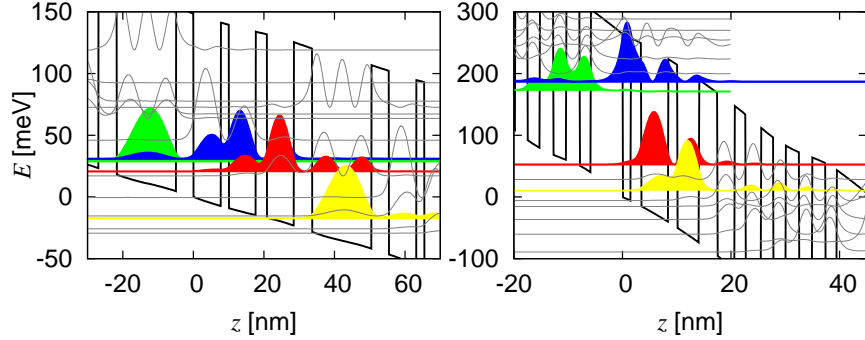


Figure 3.2: The subband structure of a THz QCL [7] on the left and a mid-IR QCL [8] on the right. The lasing transition occurs from the blue to the red subband. The green subbands are the *injector* subband designed to efficiently inject electrons in the upper laser subband via resonant tunneling at the design bias. The yellow subbands are the *ejector* subbands designed to efficiently depopulate the lower laser subbands via phonon emission. The full black lines are the heterostructure potentials plus bias,  $V_{\text{h.c.}}(z) - eFz$ , and the thin grey lines are other subbands not essential for laser action. Note that the THz device has much fewer subbands per period, *e.g.*, the ejector subband of one period is the same as the injector for the next.

Thereby, electrons will relax fast from the lower laser subband by emitting optical phonons, see Fig. 3.2.

A second feature that differs between ordinary semiconductor diode lasers and QCLs, is that the electrons are re-used in QCLs. Once the electrons enter the ejector subband they are reinjected into the upper laser subband of the neighboring quantum wells, see Fig. 3.2. This is made possible by a periodic repetition of a set of quantum wells, usually referred to as a period. Thereby, electrons may emit many photons when going through the QCL, while only one photon can be emitted per electron entering a diode laser. This periodic repetition of a set of quantum wells is clearly visible in right part of Fig. 3.1.

Most QCLs are based either on the  $\text{Al}_{0.48}\text{In}_{0.52}\text{As}/\text{Ga}_{0.47}\text{In}_{0.53}\text{As}$  material system or  $\text{Al}_x\text{Ga}_{1-x}\text{As}/\text{GaAs}$ . The first material system has a conduction band offset, or quantum well depth, of approximately 520 meV and is lattice matched to InP. In the AlGaAs/GaAs system there is a degree of freedom, AlAs and GaAs have approximately the same lattice constant and mixing these materials does not give rise to any strain. Therefore,  $x$  can in principle be any concentration between 0 and 1 and the resulting conduction band offset is

approximately  $995x$  meV for  $x \lesssim 0.5$ <sup>1</sup> [9, 10]. More exotic material systems have been proposed, mainly to reach larger conduction band offsets in order to achieve lasing at higher frequencies.

The first lasers were based on the AlInAs/GaInAs system because of its large conduction band offset, the low effective mass and the fact that InP is a suitable waveguide material. However, both alloy and interface roughness scattering are strong in this material system. In GaAs, alloy scattering is not present, and the lower conduction band offset that can be chosen in AlGaAs/GaAs diminish interface roughness scattering. Therefore, this is often the material system of choice for long wavelength, THz lasers.

### 3.2 Current Status

Since the first realization one and a half decade ago, the QCL designs have improved fast. The current wavelength span, without the use of strong magnetic fields, is from  $2.6 \mu\text{m}$  [11] to  $250 \mu\text{m}$  (1.2 THz) [12], which is almost two orders of magnitude for the same lasing principle. Also, lasing far above room temperature has been achieved [13].

Due to the strong relaxation at the LO phonon energy<sup>2</sup>, maintaining a population inversion at this specific energy has so far been unfruitful. This energy divides the QCLs into two groups: First, high frequency lasers, called *mid-IR* QCLs having lasing frequencies above the optical phonon frequency, and second, *THz* QCLs that emit radiation below this frequency.

While the mid-IR QCL is now a mature, commercially available technology, lasing up to and beyond room temperature, there is ongoing research towards higher frequencies [14]. THz lasers are, however, still bound by their low operating temperatures, which strongly restricts any potential applications. Increasing the temperature operating range of these devices is an area of intense research [15, 16], but also lasing at lower frequencies is of interest.

There are a few different design schemes for THz QCLs occurring in literature [15]. In Fig. 3.3, the designs are simply grouped into Resonant Phonon (RP) designs and other designs. The uniting feature of the other designs is that they are not based on depopulation of the lower laser subband via LO phonon emission. Instead, electrons leave the lower laser subband via tunneling and scattering into a miniband of closely separated subbands. The electrons flow via this miniband into the upper laser subband of the next period. From Fig. 3.3, it can be concluded that these other designs are favorable for lower laser frequencies but have inferior temperature performance.

---

<sup>1</sup>For  $x > 0.38$  the  $\Gamma$ -point is no longer the minimum of the conduction band [9] and transport complications will arise.

<sup>2</sup>36 meV, 8.7 THz or  $34 \mu\text{m}$  in GaAs, 50 meV in AlAs and 30 meV in InAs.

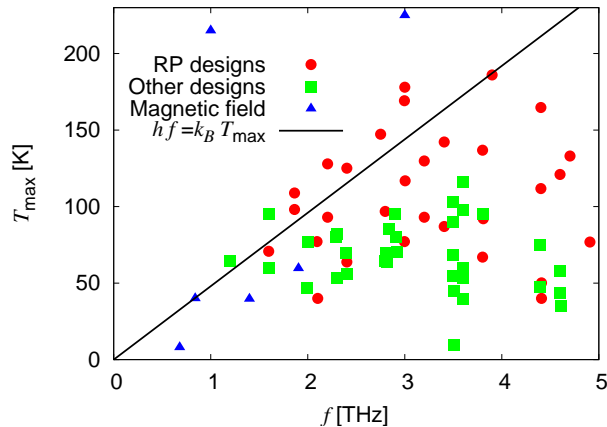


Figure 3.3: Maximum operating temperature vs. emission frequency for THz QCLs. At higher temperatures, resonant phonon designs are leading while for low frequencies other designs are favorable. There is strong ongoing research toward higher operating temperatures (up in figure) and, also, towards lower frequencies (left in figure). A magnetic field of 31 T was needed for the strongly deviating laser in the upper left corner of the figure [17]. The figure is adapted from Ref. [15] with data added from Refs. [17–20].

Resonance phonon depopulation differs slightly from standard phonon depopulation. In order to quench relaxation directly from the upper laser subband to the ejector subband by phonon emission in THz lasers, the ejector subband is shifted spatially to lower the overlap with both the lasing subbands. To maintain strong depopulation of the lower laser subband a second subband with a strong overlap with the ejector subband is put in resonance with the lower laser subband. Thus, electrons leave the lower laser subband via resonant tunneling to the energetically aligned subband and, from there, relax to the ejector subband by emitting an optical phonon. This extra subband can be seen in left part of Fig. 3.2.

A second advantage with the other, non-RP, designs is much better wall-plug efficiency [21]. This quantity is defined as the power of the outgoing laser light divided by the electric power put in the device. The rest of the power will be dissipated and heat up the device. In an absolutely ideal RP THz laser one optical phonon is emitted for every photon. The energy loss to the phonons will heat the device and therefore, the maximum wall-plug efficiency will be  $hf/(hf + E_{LO})$  or  $\sim 25\%$  at 2 THz in GaAs, which gets worse for lower frequencies. In the other designs, there are no theoretical limit for the wall-plug efficiency since the energetic width of the miniband (energy difference between the lower laser

subband and the upper laser subband of the next period) can, in principle, be made arbitrarily small. However, as scattering within the miniband is expected to be so strong that the electrons are in quasi-equilibrium, the energetical width of the miniband and the electron temperature alone determine the population inversion.

This is also the reason for the low maximum operation temperature in these devices; As the emitted photons should not be re-absorbed in the miniband, the energetic width of the miniband must be smaller than  $hf$ . Currently, an optimized non-RP THz QCL has a wall-plug efficiency of 2.4 % [22] while the corresponding figure is 0.6 % for RP designs [23]. In this thesis only RP-designs are studied, so unless explicitly mentioned, THz QCL will refer to RP THz QCL.

In order to turn these different designs into working lasers they need to be paired up with some waveguide that confine the laser light field to the gain material while, at the same time, absorb as little energy as possible. This is a research field on its own and will not be discussed here.

An alternative approach to obtain THz emission is to design a mid-IR device that emits light at two frequencies. THz emission can then be generated by difference frequency generation inside the laser device. Emission has been observed up to room temperature [16]. However, the poor conversion efficiency of the nonlinear process gives an output power of only  $3 \mu\text{W}$ .

# 4

## Heterostructures

Semiconductors are characterized by a finite energy gap between states filled by electrons, the so-called valance band, and empty available states, the conduction band. This band gap is often of the order of the energy of a photon in the visible region of the electromagnetic spectrum, which is the feature employed in most opto-electronic devices. As the size of the gap is relatively small, the conductivity of the semiconductor can be controlled by external voltages or doping, which is key feature of building block of computers, the transistor.

This thesis deals with the physics of electrons in the conduction band only. In bulk semiconductor the energy of an electron in the bottom of the conduction band can be written as

$$E(\vec{k}) = \frac{\hbar^2 |\vec{k} - \vec{k}_0|^2}{2m^*} + E_c, \quad (4.1)$$

where  $\vec{k}$  is the 3-dimensional crystal wave vector,  $\vec{k}_0$  is the wave vector at the bottom of the conduction band,  $m^*$  is the effective mass determined by the curvature of the conduction band at  $\vec{k}_0$ , and  $E_c$  is the energy of the conduction band at  $\vec{k}_0$ . In the semiconductors relevant here, the bottom of the conduction band is the  $\Gamma$ -point, where  $\vec{k}_0 = 0$ . This is not the case in, *e.g.*, the popular material for electronics, silicon. In general the (inverse) effective mass will be a tensor. However, the high symmetry of the crystal at the  $\Gamma$ -point results in an isotropic effective mass. The effective mass is generally much lower than the free electron mass.

The wavefunctions in the conduction band for bulk materials are Bloch functions, given by Bloch's theorem [24],

$$\varphi_{\vec{k}}(\vec{r}) = e^{i\vec{k}\cdot\vec{r}} u_{\vec{k}}(\vec{r}), \quad (4.2)$$

where  $u_{\vec{k}}(\vec{r})$  is a fast oscillating lattice periodic function. Close to the  $\Gamma$ -point a common approximation is  $u_{\vec{k}}(\vec{r}) \approx u_{\vec{k}_0}(\vec{r})$  and, thus, the Bloch functions, Eq. (4.2), show strong similarities to plane waves, on a long length scale.



## 4.1 Heterostructures – Quantum Wells

Different types of semiconductors can be grown in layers, a structure known as heterostructure. Each layer has a certain conduction band energy and effective mass. An often used approximation in these type of systems is the envelope function approximation [25], where the system is described, in the growth direction, by the Hamiltonian [26],

$$\hat{H} = -\frac{\hbar^2}{2} \frac{d}{dz} \frac{1}{m^*(z)} \frac{d}{dz} + V_{\text{h.s.}}(z), \quad (4.3)$$

where the layers have been grown in the  $z$ -direction. The effective mass and the heterostructure potential,  $V_{\text{h.s.}}(z)$ , are material dependent and therefore  $z$  dependent in a step-like manner. The eigenstates of the Hamiltonian are the envelope functions. The planewave form of the envelope function in Eq. (4.2) suggests that the eigenstates of the full heterostructure Hamiltonian, including the ionic potential, are the envelope functions together with the lattice periodic function,  $u_{\vec{k}}(\vec{r})$ . The effective mass has been placed between the two spatial derivatives in order to have a hermitian Hamiltonian, although there is an ongoing discussion regarding the correct form of the kinetic energy with spatially dependent mass, see, *e.g.*, Refs. [27,28]. Most ambiguities comes from fact that the boundary conditions for the envelope functions are not well defined, such as for the full wavefunction.

A simple, but interesting, heterostructure is the quantum well, where a thin layer of a material with a low conduction band energy,  $E_c$ , is sandwiched between barrier material with larger conduction band energy. This potential structure will localize electrons in the  $z$ -direction, with the resulting envelope function,

$$\Psi_{\mathbf{k}}^n(\vec{r}) = \frac{e^{i\mathbf{k}\cdot\mathbf{r}}}{\sqrt{A}} \psi_n(z), \quad (4.4)$$

where bold quantities are two-dimension vectors in the plane of the quantum well,  $A$  is the normalizing area of the structure and  $\psi_n(z)$  the envelope function in the growth direction. The  $n$ -index corresponds to different subbands in the quantum well. The corresponding energy is

$$E_{n\mathbf{k}} = E_n + \frac{\hbar^2 |\mathbf{k}|^2}{2m^*}, \quad (4.5)$$

where  $E_n$  is eigenenergy of the one dimensional Hamiltonian, Eq. (4.3), and the second terms is the in-plane kinetic energy. As the envelope functions overlap both well and barrier material the choice of effective mass is not straight forward. However, as the envelope functions mainly reside in the well material, this effective mass is often chosen. The parabolic energy dispersion is known as

a *subband* and is central in this thesis. The density of states for each subband is constant in energy,

$$\rho_n(E) = \frac{m^*}{\pi\hbar^2} \theta(E - E_n). \quad (4.6)$$

A further complication in these heterostructures is that the mass is energy dependent. In the effective mass approximation the conduction band is Taylor expanded in wave vector, and the second order term, or the curvature, corresponds to the effective mass. Close to the  $\Gamma$ -point this is an excellent approximation. However, in many mid-IR lasers, such as the one studied in Paper I, quite high energies are involved, and accordingly, the effective mass needs to be adjusted. At higher energies, the conduction band becomes more flat and the effective mass increases. To capture this energy dependence the following expression is used (see Ref. [29] or Eq. (49), Chap. 1 in Ref. [25])

$$m^*(E) = m^* \left( 1 + \frac{E - E_c}{E_g} \right), \quad (4.7)$$

where  $m^*$  is the effective mass at the  $\Gamma$ -point and  $E_g$  is the band gap of the material. The energy scale on which the effective mass changes is the band gap energy, of the order of 1 eV in most materials, and is relatively large compared to the energy scale of subbands in the quantum wells. Thus, the resulting Hamiltonian used throughout this work for evaluating the envelope functions in the  $z$ -direction is

$$\hat{H} = -\frac{\hbar^2}{2} \frac{d}{dz} \frac{1}{m^*(z, E)} \frac{d}{dz} + V_{\text{h.s.}}(z). \quad (4.8)$$

The term envelope function will be dropped for the more commonly used term wavefunction.

## 4.2 Periodic Structures – Superlattices

The laser structures studied in this thesis consist of sets of quantum wells, repeated on the order of hundred times, a system known as *superlattice*. This periodicity in the growth direction gives a certain form of the solutions to Eq. (4.8). By the use of Bloch's theorem the solutions can be written as

$$\varphi_q^\nu(z) = e^{iqz} u_q^\nu(z), \quad (4.9)$$

where  $\nu$  refers to different *minibands*,  $q$  is the wave vector in the growth direction,  $u_q^\nu(z) = u_q^\nu(z + d)$  is the superlattice periodic function and  $d$  is the period length of the superlattice. The corresponding energies form minibands. Note that previously Bloch's theorem was used for a periodic array of ions resulting in the valance and conduction band, and here, a periodic array of quantum

wells gives rise to minibands *within* the conduction band. The main difference is that normal crystals are given by Nature, while here, the periodic potential,  $V_{\text{h.s.}}(z)$ , is controlled by the grower. These interesting systems, similar to quantum cascade lasers but simpler, are studied in more detail in the field of superlattices [30]. It should be noted, however, that the simplest working quantum cascade laser has only two quantum wells per period [20].

The Bloch functions in Eq. (4.9) are infinitely extending and are therefore not suitable for numerical computations. Even analytically, infinitely extending states can give rise to problems with negative spectral functions, see Chap. 11.2 in Ref. [31] and references therein. Instead, the Bloch functions can be transformed to localized *Wannier*-functions,

$$\Psi^\nu(z - nd) = \sqrt{\frac{d}{2\pi}} \int_{-\pi/d}^{\pi/d} dq e^{-inqz} \varphi_q^\nu(z). \quad (4.10)$$

These states are not eigenstates of the Hamiltonian, but are localized and orthonormal, and each state, periodically translated, spans a full miniband. The trick here is to choose the phase of the Bloch functions,  $\varphi_q^\nu(z)$ , to get a strongly localized Wannier functions, see, *e.g.*, Ref. [32].

Under operating conditions, strong static electric fields are applied to the heterostructures, which break the translation invariance, resulting in a Hamiltonian of the form

$$\hat{H} = -\frac{\hbar^2}{2} \frac{d}{dz} \frac{1}{m^*(z, E)} \frac{d}{dz} + V_{\text{h.s.}}(z) - eFz, \quad (4.11)$$

where  $e < 0$  is the electron charge and  $F$  the electric field. Mathematically, the electric field gives rise to problems; The Hamiltonian is not bounded from below and this will result in a continuous energy spectrum [33]. However, for any approximate eigenstate  $\Psi(z)$  with energy  $E$ , there will be infinitely many similar states  $\Psi(z - nd)$  with energy  $E - eFdn$ , where  $n$  is an arbitrary integer. This structure is known as the Wannier-Stark ladder. In order to find these approximate eigenstates, the Hamiltonian in Eq. (4.11) is diagonalized including a few Wannier states per period and a few periods, and the central wavefunctions are chosen as approximate *Wannier-Stark* states. For a typical THz laser  $\sim 5$  states/period are chosen and  $\sim 15$  for a mid-IR laser, and states from three periods are usually diagonalized. An alternative to the approach described above is to solve Eq. (4.11) for one or a few periods and choose the resulting states as basis states.

There are, however, a few advantages with the scheme described above. By including a certain number of Wannier states one can be sure to fully span the Hilbert space up to a certain energy. Even further, this energy can be higher than the height of the barriers, an energy region where the electrons are unbound. These states are difficult to obtain correctly by simply solving

Eq. (4.11) are important in Paper I where absorption to these high energy states is discussed.

In the transport calculation, the average potential from the ionized dopants and mean-field electron-electron interaction, which also are periodic in the growth direction, are included in  $V_{h.s.}(z)$ . This, however, has to be calculated self-consistently.

Calculating the properties of quantum well structures, such as the QCL, can usually be divided into three different tasks. First, the eigenstates and eigenenergies of the heterostructure potential are calculated by solving the Schrödinger equation. Once the wavefunctions are known, the occupation of these states and the current are calculated via some transport method. Finally, to obtain the optical laser characteristics, the response to an electromagnetic field is calculated.

The first part of the calculations was discussed above. The periodicity of these structures together with the static electric field gives rise to some complications, as described above, but can be solved by certain approximation schemes. The second step, the transport calculation, is needed to obtain the current and distribution of electron, will be addressed in Chap. 6. There are, however, transport implementations that do not require any basis states and are instead spatially meshed in the  $z$ -direction [34]. And, at last, the optical properties are calculated via the response to an oscillating electromagnetic field, as described in Chap. 8.



# 5

## Scattering Mechanisms

Independent of calculation method, including the important scattering mechanisms is crucial to correctly model the transport properties of QCLs. In order to understand the operational state of the QCL and to further optimize its performance, knowledge about the features of the different scattering mechanisms is necessary. The dominant scattering mechanisms are summarized in Tab. 5.1.

### 5.1 Phonon Scattering

Scattering with longitudinal optical phonons is an important scattering mechanism in most QCLs. The most common scheme to reach a high depletion rate from the lower laser subband is to tailor the conduction band profile such that an ejector subband is located one optical phonon energy below. This situation causes the electrons in the lower laser subband to relax down the ejector subband by emitting optical phonons. This scheme is referred to as the phonon depopulation scheme and is used frequently in both THz and mid-IR

<i>Scattering Mechanism</i>	<i>Elastic</i>	<i>Temp. dep.</i>	<i>Comment</i>
Optical phonon	No	Yes	Dominant relax. proc.
Acoustic phonon	No	Yes	Weak
Ionized impurity	Yes	No <sup>a</sup>	
Interface roughness	Yes	No	Growth & material dep.
Alloy disorder	Yes	No	Material dep.
Electron-electron	Yes/No <sup>b</sup>	Yes/No <sup>a</sup>	

Table 5.1: The most common scattering mechanisms in QCLs.

<sup>a</sup>Both impurity and electron-electron scattering are temperature independent. However, in most approximations regarding the screening, an effective electron temperature enters.

<sup>b</sup>Since electron-electron scattering is a many-body effect each electron might lose and gain energy, however, the total energy of the electron gas is conserved at each scattering event.

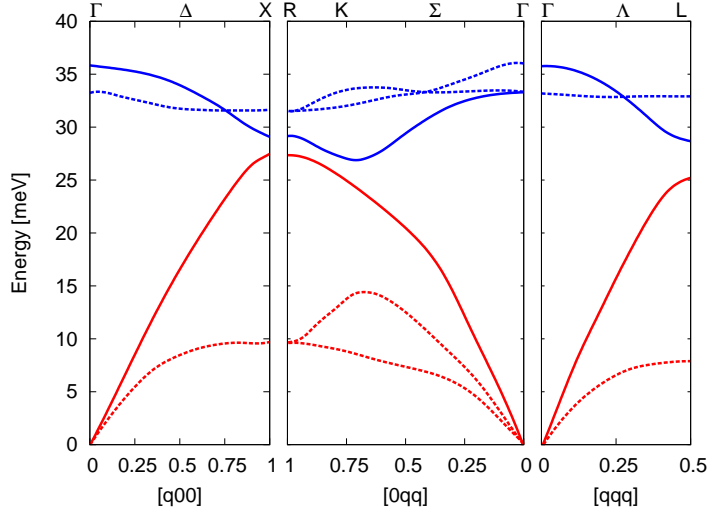


Figure 5.1: Phonon dispersion in GaAs obtained by inelastic neutron scattering. Red lines show the acoustic phonon branches and blue show optical branches. Full lines correspond to longitudinal and dashed to transverse polarization. In the calculation only the longitudinal phonons (full lines) are taken into account. The optical phonon dispersion is approximated by a constant at 36 meV and the acoustic with a linear dispersion with a slope corresponding to the sound velocity. The phonon wave vector is given in dimensionless units. The typical electron wave vector on this scale is much smaller,  $k_{\text{typ}}^e \approx 0.02$ . The figure is adapted from Ref. [35].

devices. The dispersion of optical phonons is approximately constant and close to 36 meV in GaAs, see Fig. 5.1.

Acoustic phonons are only weakly coupled to electrons and this scattering mechanism is often omitted in calculations. However, although the coupling between electrons and acoustic phonons is relatively weak, it constitutes the only coupling to the lattice at energies below the optical phonon energy and can be crucial to thermalize the electron gas and couple it to the lattice temperature. Acoustic phonon scattering is also more difficult to include in calculations compared to optical phonon scattering due to the linear dispersion, instead of the constant dispersion for optical phonons, see Fig. 5.1. A detailed derivation of a self-energy for acoustic phonon scattering, and a study of its importance in RP THz QCLs, can be found in Paper III.

The Hamiltonian describing electron-phonon interaction can be written as

$$\hat{H}_{e\text{-ph}} = \sum_{\alpha\beta\mathbf{k}} \sum_{qz\mathbf{q}} g(\vec{q}) M_{\alpha\beta}(qz) \hat{a}_{\alpha,\mathbf{k}+\mathbf{q}}^\dagger \hat{a}_{\beta,\mathbf{k}} \left[ \hat{b}_{\vec{q}} + \hat{b}_{-\vec{q}}^\dagger \right], \quad (5.1)$$

where  $\hat{b}_{\vec{q}}$  ( $\hat{b}_{\vec{q}}^\dagger$ ) annihilates (creates) a phonon with 3-dimensional wave vector  $\vec{q}$ ,  $M_{\alpha\beta}(qz) = \int dz \psi_\alpha^*(z) e^{iqz} \psi_\beta(z)$  and  $g(\vec{q})$  is the coupling strength. Longitudinal acoustic phonons (full red lines in Fig. 5.1) cause time and space varying contractions and elongation of the lattice and couple to electrons via the deformation potential. The corresponding coupling strength is

$$|g(\vec{q})|^2 = \frac{E_{\text{ph}} D^2}{2\rho V v^2}, \quad (5.2)$$

where  $E_{\text{ph}}$  is the phonon energy,  $D$  is the deformation potential, *i.e.*, the change in the conduction band energy due to deformation,  $\rho$  is the mass density, and  $v$  is the speed of sound in the material, corresponding to the slope of the dispersion. In our current model, the acoustic phonon energy is set, for simplicity, to be a constant close to  $k_B T$ .

Optical phonons in polar materials, such as the ones used for QCLs, cause an oscillating polarization of the material with a coupling to electrons described by

$$|g(\vec{q})|^2 = \frac{E_{\text{ph}} e^2 (\varepsilon_r - \varepsilon_\infty)}{2\varepsilon_r \varepsilon_\infty \varepsilon_0 V q^2}, \quad (5.3)$$

where  $\varepsilon_r$  is the relative dielectric constant of the semiconductor material,  $\varepsilon_\infty$  is the high frequency relative dielectric constant, and  $\varepsilon_0$  the permittivity of free space. This form is known as the Fröhlich coupling [36].

The phonon emission rate is proportional to  $n_B(E_{\text{ph}}) + 1$  where  $n_B(E)$  is the Bose-Einstein distribution function,  $(e^{E/k_B T} - 1)^{-1}$ , and  $E_{\text{ph}}$  is the phonon energy. The  $n_B(E_{\text{ph}})$  term is due to stimulated phonon emission and the 1 corresponds to spontaneous emission. The strong temperature dependence of phonon emission starts when stimulated emission dominates over spontaneous emission, *i.e.*,  $n_B(E_{\text{ph}}) \approx 1$  or  $E_{\text{ph}} \approx k_B T$ . For an optical phonon energy of 36 meV this temperature equals 420 K. Therefore, the temperature dependence of the optical phonon scattering is expected to be negligible for THz lasers operating close to 200 K.

The phonons are assumed to be bulk-like, although the QCL consists of many thin layers of different materials. In ternary alloys, such as  $\text{Al}_{0.15}\text{Ga}_{0.85}\text{As}$ , most material parameters are well estimated by the weighted average between AlAs and GaAs. This is not the case for the phonon frequencies, where instead both the phonon frequency of AlAs and GaAs is expected to be present [37]. However, due to the low Al concentration in most THz QCLs, only a low fractions of the phonon modes will be AlAs-like. In bulk  $\text{Al}_x\text{Ga}_{1-x}\text{As}$ , the



AlAs-like phonon modes becomes dominant for  $x \approx 0.4$ . The lighter Al ions have higher phonon frequency,  $E_{LO}^{\text{AlAs}} = 50$  meV, and hence a stronger coupling, see Eq. (5.3).

More important than the frequency of the phonons is the overlap with the electronic states [38,39]. As the AlAs-like modes are, to a large extent, localized to the barriers, and the electrons to the quantum wells, these modes are expected to play a minor role. Also, taking localized and interface phonon modes into account in transport calculation would very much complicate matters.

## 5.2 Impurity Scattering

In order to get a high and controlled electron concentration in QCLs certain regions of the laser period are doped. These doping atoms lose one electron each and become ionized. The result is a background charge density of ions, randomly located, which breaks the in-plane translation invariance and therefore gives rise to scattering [40].

The potential from an ionized dopant is proportional to one over the distance. Due to the long-range nature of this potential screening becomes important. This will lower the magnitude of the potential at long distances and the effective potential from an ion located at  $\vec{r}_i$ , reads

$$V_{\text{eff}}^i(\vec{r}) = \frac{e^2}{4\pi\epsilon_0\epsilon_r} \frac{e^{-\lambda|\vec{r}-\vec{r}_i|}}{|\vec{r}-\vec{r}_i|}, \quad (5.4)$$

where  $\lambda$  is the inverse screening length. The screening of ionized dopants is central in this work, and a more detailed discussion can be found in Chap. 7 as well as in Papers II and V.

## 5.3 Interface Roughness Scattering

The interface between two materials can be made atomically sharp, meaning that the change from one material to the other is between two neighboring atomic layers. However, while the interface might be sharp and well defined, it is not flat, see right side of Fig. 5.2. This breaks the in-plane translation invariance and is taken into account by interface roughness scattering. Here, the interface is assumed to be sharp, but the location in the growth direction fluctuates randomly. The deviation of an interface from its expected position is described by the random function  $\xi(\mathbf{r})$  with the following statistical properties

$$\begin{aligned} \langle \xi(\mathbf{r}) \rangle &= 0, \\ \langle \xi(\mathbf{r})\xi(\mathbf{r}') \rangle &= \eta^2 e^{-|\mathbf{r}-\mathbf{r}'|/\lambda}, \end{aligned} \quad (5.5)$$

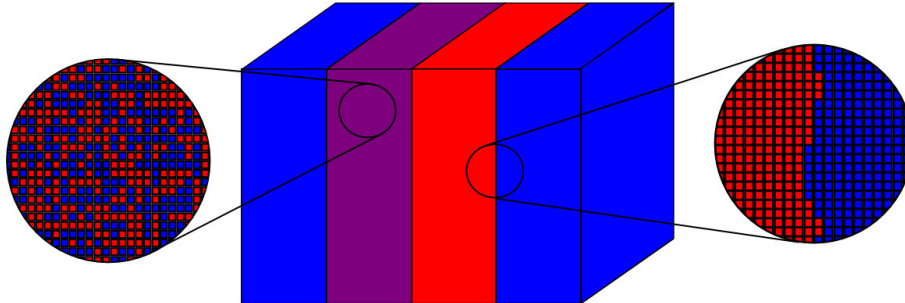


Figure 5.2: Sketch of a AlAs/Al<sub>0.5</sub>Ga<sub>0.5</sub>As/GaAs/AlAs structure. *Left:* The Al<sub>0.5</sub>Ga<sub>0.5</sub>As is not a homogeneous material, but a random mixture GaAs and AlAs. This random potential will give rise to alloy scattering. *Right:* The interfaces between to materials are not flat, they usually deviates from the average interface position by an atomic layer,  $\eta \sim 1 \text{ \AA}$ , and the fluctuation have a typical length scale of  $\lambda \sim 10 \text{ nm}$  in the in-plane direction. This will give rise to interface roughness scattering.

where  $\eta$  is the average fluctuation strength, often of the order of one atomic layer, and, here,  $\lambda$  is the correlation length. Other correlation functions than the exponential can be found in the literature, such as Gaussians [34,41]. Correlations between neighboring interfaces are often neglected, although this is questionable for very thin layers. Since the scattering is due to fluctuations of positions of the interfaces, the magnitude of the scattering depends on the conduction band offset. Therefore, this scattering mechanism is smaller in THz devices due to the smaller conduction band offset compared to mid-IR devices. In mid-IR devices, this scattering mechanism is dominant and alone determines the linewidth of the laser [42]. Some simulation has also shown that this is the dominant scattering mechanism in THz QCLs [34].

The fluctuating well widths can in principle localize electrons to regions where the quantum well is extra wide and, therefore, interface roughness should not be treated perturbatively. If a particle in a 3D box is considered, the energy is proportional to  $l_x^{-2} + l_y^{-2} + l_z^{-2}$ . The particle will localize if the energy reduction of a wider well,  $l_z \rightarrow l_z + 2\eta$ , is greater than energy gain for localizing in the plane,  $l_{x,y} = \infty \rightarrow l_{x,y} = \lambda$ . This results in that it is energetically favorable to localize in the plane if

$$l_z < \sqrt[3]{2\eta\lambda^2}, \quad (5.6)$$

which for common parameters,  $\eta \sim 1 \text{ \AA}$  and  $\lambda \sim 10 \text{ nm}$ , gives an upper limit for the quantum well width of  $\sim 3 \text{ nm}$ . Most wavefunctions and quantum wells are much wider, and also, at very thin quantum wells strong correlation between

neighboring interfaces is expected, which would reduce the risk of localization even further. An excellent text on the theory of localization due to scattering potentials in semiconductors can be found in Chap. 7.1 of Ref. [43].

## 5.4 Alloy Scattering

The binary III-V semiconductor materials used in QCLs are obtained by mixing materials from group III in the periodic system (aluminum (Al), gallium (Ga), indium (In)) with materials from group V (phosphorus (P), arsenic (As), antimony (Sb)). This, however, only gives a discrete number of materials since the density of atoms of both groups must be equal. Even further, only a few of these are lattice matched. Mixing two binary alloys gives a ternary alloy. For instance, mixing AlAs and GaAs gives  $\text{Al}_x\text{Ga}_{1-x}\text{As}$  where  $0 \leq x \leq 1$ . Material parameters, such as effective mass, band gap and conduction band offset, for the new material are usually linearly interpolated from its two constituent binary alloys. In some situation linearly interpolated parameters do not describe the ternary alloy well and bowing parameters must be taken into account. These usually have the form  $Cx(1-x)$  and can be found for most III-V alloys in Ref. [9].

This interpolation scheme is, however, not entirely correct. In  $\text{Al}_{0.5}\text{Ga}_{0.5}\text{As}$  for example, half of the crystal molecules are AlAs and half are GaAs. The spatial distribution of these different crystal molecules are random and will therefore give rise to scattering [44, 45]. A common way of minimizing alloy scattering in QCLs is to choose GaAs for the well material and  $\text{Al}_x\text{Ga}_{1-x}\text{As}$  for the barriers. Most electronic states have small overlap with the barrier material, and therefore, alloy scattering becomes negligible compared to other scattering mechanisms. Therefore, this is the material system of the optimized lasers studied in Papers II-V.

A common approach is to treat alloy scattering in a ternary alloy of two constituents, material  $A$  and  $B$ , as a random perturbing potential with one value at regions of  $A$  and another at regions of  $B$ ,

$$V^i(\vec{r}) = \begin{cases} x\Delta V f(\vec{r} - \vec{r}_i) & \text{with probability } 1-x \\ -(1-x)\Delta V f(\vec{r} - \vec{r}_i) & \text{with probability } x \end{cases}, \quad (5.7)$$

where  $\Delta V = E_c^A - E_c^B$  is the conduction band offset of material  $A$  and  $B$ ,  $f(\vec{r})$  is equal to one inside the volume of a molecule of  $A$  or  $B$  located at the origin and zero elsewhere. Since there are four Ga or Al atoms per unit cell the size of the molecule is one fourth of the volume of the unit cell. Also, since the dimension of the electron wavefunction is much larger than the lattice constant,  $f(\vec{r})$  is often approximated by a  $\delta$ -function,  $f(\vec{r}) \approx (a^3/4)\delta^3(\vec{r})$ , where  $a$  is the lattice constant. The  $\delta$ -function gives a simple, wave vector independent scattering potential where the matrix element only depends on the

wavefunction overlap. The material composition of neighboring unit cells is assumed to be uncorrelated, although the fitting of phonon modes to reflectivity measurements suggests some clustering [46].

## 5.5 Electron-Electron Scattering

All previous scattering mechanisms have involved a single electron interaction with a scattering potential or a phonon bath. Electron-electron (e-e) scattering differs since here, two electrons are involved. This causes an increased numerical complexity, and therefore, up until recently, this scattering mechanism has only been included in simpler rate equation and Monte Carlo transport models.

Physically, e-e scattering is important for thermalization [47], as this is the only scattering mechanism that facilitates direct energy exchange between the particles. This scattering mechanism is especially important in non-RP THz laser, which are designed such that optical phonon emission is quenched due to small energy differences between subbands. Scattering within and between the closely spaced subbands in the miniband is expected to be by large extent determined by e-e scattering. These devices are typically employed for low frequency operation at low temperatures, see Fig. 3.3, a situation where a closed expression for the e-e scattering rate can be obtained [48]. It is found that e-e scattering, from the upper to the lower laser subband, increases strongly with smaller energy separation. However, the rate strongly depends on the wavefunction symmetry.

In the transport implementation used in Papers II-IV, e-e scattering is neglected. To phenomenologically remedy this lack of thermalization for the carriers the coupling to the acoustic phonons can be increased. This will however not only thermalize the electron gas but also cool it, while a more detailed Monte Carlo calculation has shown that e-e scattering heats the gas [47]. Also, for the device presented in Ref. [7] the discrepancy between the experimental and simulated current-voltage relation increases with increased coupling to acoustic phonons, see Paper III.

With strong approximations, e-e scattering has recently been implemented in Non-Equilibrium Green's Function transport calculations. In Ref. [34], e-e scattering is included within the GW-approximation [49] where the screened e-e interaction is approximated by the corresponding static scattering potential for an isotropic 3D electron gas at thermal equilibrium. Alternatively, in Ref. [50], the GW-approximation is also employed, but with the plasmon pole approximation instead, resulting in dynamic screening.



# 6

## Transport Models

As discussed in Chap. 4, electrons in QCL are confined by the heterostructure potential in the growth direction, defined here as the  $\vec{z}$ -direction, and are free to move in the  $\vec{x}\vec{y}$ -plane. The translational invariance in the  $\vec{x}\vec{y}$ -plane suggests the suitable form of the basis states,

$$\Psi_{n\mathbf{k}}(z, \mathbf{r}) = \psi_n(z) \frac{e^{i\mathbf{k}\cdot\mathbf{r}}}{\sqrt{A}}, \quad (6.1)$$

where  $n$  is the subband index,  $\mathbf{r}$  and  $\mathbf{k}$  are 2-dimensional vectors in the normal and reciprocal  $\vec{x}\vec{y}$ -plane, respectively, and  $A$  is the normalizing area.

The Hamiltonian describing the system is split up,

$$\hat{H} = \hat{H}_0 + \hat{H}_{\text{scatt}}, \quad (6.2)$$

where  $\hat{H}_0$  is diagonal in  $\mathbf{k}$  and  $\hat{H}_{\text{scatt}}$  contains all scattering mechanisms which break the translational invariance in the  $\vec{x}\vec{y}$ -plane and therefore couple states with different in-plane wave vector,  $\mathbf{k}$ . The form of  $\hat{H}_0$  is

$$\begin{aligned} \hat{H}_0 &= \sum_{m,n,\mathbf{k}} U_{mn\mathbf{k}} \hat{a}_{m\mathbf{k}}^\dagger \hat{a}_{n\mathbf{k}}, \\ U_{mn\mathbf{k}} &= U_{mn} + \frac{\hbar^2 \mathbf{k}^2}{2m^*} \delta_{mn}, \end{aligned} \quad (6.3)$$

where  $\hat{a}_{n\mathbf{k}}$  ( $\hat{a}_{n\mathbf{k}}^\dagger$ ) is the annihilation (creation) operator corresponding to subband  $n$  and in-plane wave vector  $\mathbf{k}$ , and  $U_{mn}$  is the matrix element including the heterostructure potential, the mean-field electron-electron and electron-dopant interaction, as well as applied electric field. The scattering part of the Hamiltonian,  $\hat{H}_{\text{scatt}}$ , is treated perturbatively via scattering rates or so-called self-energies, as described below.

### 6.1 Rate Equations

The simplest approach to transport is rate equations [51]. Here, one starts with the eigenstates of the heterostructure potential and calculates the scattering

rates between the states using Fermi's Golden Rule,

$$\Gamma_{n\mathbf{k}\rightarrow n'\mathbf{k}'} = \frac{2\pi}{\hbar} |\langle n', \mathbf{k}' | H_{\text{scatt}} | n, \mathbf{k} \rangle|^2 \delta(E_{n\mathbf{k}} - E_{n'\mathbf{k}'} \pm \Delta E), \quad (6.4)$$

where  $\Delta E$  is either 0 for elastic scattering or the phonon energy for phonon scattering. The rates between subbands are then calculated via

$$\Gamma_{n\rightarrow n'} = \sum_{\mathbf{k}, \mathbf{k}'} f_{n, \mathbf{k}} \Gamma_{n\mathbf{k}\rightarrow n'\mathbf{k}'} (1 - f_{n', \mathbf{k}'}), \quad (6.5)$$

where  $f_{n, \mathbf{k}}$  are momentum resolved occupations, such that

$$n_n = (2/A) \sum_{\mathbf{k}} f_{n, \mathbf{k}}. \quad (6.6)$$

The key simplification is that only subband populations  $n_n$  are calculated, and not the momentum resolved occupations, which are assumed to be Fermi-Dirac distributions in Eq. (6.5).

Finally, the task is to find the stationary occupations  $n_n$ , which are the solution to

$$\frac{dn_n}{dt} = - \sum_{n'} \Gamma_{n\rightarrow n'} n_n + \sum_{n'} \Gamma_{n'\rightarrow n} n_{n'}, \quad (6.7)$$

when the time derivative is set zero with the constraints that  $\sum_n n_n = n_{\text{tot}}$  and all  $n_n \geq 0$ . This equation can easily be solved once the scattering rates are evaluated.

The advantage of choosing a simple model is that solutions can be found fast and also, that it is possible to include very many scattering mechanisms, even complex electron-electron scattering. Due to the many parameters in QCL design, such as barrier and well widths and bias, a fast transport implementation is favorable for optimization.

## 6.2 Monte Carlo Method

Solving the rate equations for the momentum resolved occupations,  $f_{n, \mathbf{k}}$  instead of the subband populations  $n_n$  by simply inverting the rate equations is numerically demanding. Instead, the Monte Carlo method can be employed [52, 53]. Here, the approach is quite different, a few electrons are followed in time while random scattering events occur. Each scattering event is treated randomly with probability proportional to the corresponding scattering rate. After a certain time, the occupations  $f_{n, \mathbf{k}}$  can be estimated via the time averaged occupation of the different states.

A simplification used in Refs. [52, 53] is using momentum independent scattering matrix elements when calculating the scattering rates,

$$\Gamma_{n\mathbf{k}\rightarrow n'\mathbf{k}'} = \frac{2\pi}{\hbar} |\langle n' | H_{\text{scatt}} | n \rangle|^2 \delta(E_{n\mathbf{k}} - E_{n'\mathbf{k}'} \pm \Delta E), \quad (6.8)$$

where the momentum dependence comes from the energy conserving  $\delta$ -function.

### 6.3 Density Matrix Theory

In order to improve the semi-classical methods described above, the so-called coherences, or polarizations, are included,  $\langle \hat{a}_{m\mathbf{k}}^\dagger \hat{a}_{n\mathbf{k}} \rangle$  where  $m \neq n$ . These are put in a matrix,

$$\rho_{nm}(\mathbf{k}) = \langle \hat{a}_{m\mathbf{k}}^\dagger \hat{a}_{n\mathbf{k}} \rangle, \quad (6.9)$$

where the diagonal elements correspond to the occupations,  $f_{n\mathbf{k}} = \rho_{nn}(\mathbf{k})$ . This is the reason for the name, the density-matrix method [54, 55]. The dynamics is described by the von Neumann equation,

$$\frac{\partial \rho}{\partial t} = \frac{1}{i\hbar} [H, \rho], \quad (6.10)$$

where  $[a, b] = ab - ba$ . The solution to  $[H, \rho] = 0$  is the stationary state of the QCL system [56, 57].

Once the density matrix is found the expectation value of any operator,  $A$ , can be found via,

$$\langle A \rangle = \text{Tr}[A\rho], \quad (6.11)$$

where  $\text{Tr}[\cdot]$  is the trace, in this system  $\sum_{n,\mathbf{k}} \langle n, \mathbf{k} | \cdot | n, \mathbf{k} \rangle$ .

### 6.4 Non-Equilibrium Green's Functions

To study the QCL system, the formalism of Non-Equilibrium Green's Functions (NEGF) can be used [31, 58, 59]. This method has successfully been applied to analyze and describe superlattices [30] and QCLs by different groups [34, 60–63]. The central quantity is the lesser Green's function or correlation function, defined by

$$G_{mn}^<(\mathbf{k}; t_m, t_n) = i \langle \hat{a}_n^\dagger(\mathbf{k}, t_n) \hat{a}_m(\mathbf{k}, t_m) \rangle, \quad (6.12)$$

also called the particle propagator. Due to the translational invariance in the  $\vec{x}\vec{y}$ -plane, the Green's functions are diagonal in  $\mathbf{k}$ . Similarly, the retarded and advanced Green's function are defined as

$$G_{mn}^{\text{ret}}(\mathbf{k}; t_m, t_n) = -i\theta(t_m - t_n) \langle \{ \hat{a}_m(\mathbf{k}, t_m), \hat{a}_n^\dagger(\mathbf{k}, t_n) \} \rangle, \quad (6.13)$$

$$G_{mn}^{\text{adv}}(\mathbf{k}; t_m, t_n) = i\theta(t_n - t_m) \langle \{ \hat{a}_m(\mathbf{k}, t_m), \hat{a}_n^\dagger(\mathbf{k}, t_n) \} \rangle, \quad (6.14)$$



where  $\theta(t) = 0$  for  $t < 0$  and  $\theta(t) = 1$  for  $t > 0$ . Furthermore,  $\{a, b\} = ab + ba$  is the anti-commutator. The external potential in the studied system is assumed to be constant in time. Therefore, the Green's functions are only functions of the difference between  $t_m$  and  $t_n$  and working with the Fourier transform is more suitable

$$G_{mn}(\mathbf{k}, E) = \frac{1}{\hbar} \int dt e^{iEt/\hbar} G_{mn}(\mathbf{k}; t + t_0, t_0). \quad (6.15)$$

The lesser Green's function can be related to the better known density matrix by

$$\rho_{mn}(\mathbf{k}) = -i \int \frac{dE}{2\pi} G_{mn}^<(\mathbf{k}, E), \quad (6.16)$$

*i.e.*, the lesser Green's function can be interpreted as an energy resolved density matrix. From this expression, expectation values of any observable can be calculated from Eq. (6.11). The energy-broadening is due to the time-energy uncertainty,

$$\Delta t \cdot \Delta E \approx \hbar \quad (6.17)$$

where  $\Delta t$  is approximately the lifetime of an electron in a specific state and  $\Delta E$  is a measure of the broadening.

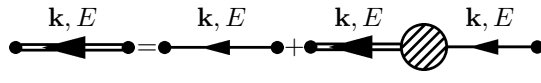
The derivation of the equations of motion for the Green's functions can be found in Ref. [30]. The result is the Dyson equation<sup>1</sup>

$$\sum_{\alpha} [E - H_{m\alpha}^0(\mathbf{k}) - \Sigma_{m\alpha}^{\text{ret}}(\mathbf{k}, E)] G_{\alpha n}^{\text{ret}}(\mathbf{k}, E) = \delta_{mn}, \quad (6.18)$$

and the Keldysh relation

$$G_{mn}^<(\mathbf{k}, E) = \sum_{\alpha, \beta} G_{m\alpha}^{\text{ret}}(\mathbf{k}, E) \Sigma_{\alpha\beta}^<(\mathbf{k}, E) G_{\beta n}^{\text{adv}}(\mathbf{k}, E), \quad (6.19)$$

where  $\delta_{nm}$  is the Kronecker delta function and  $\Sigma_{mn}(\mathbf{k}, E)$  are the self-energies that take into account the different scattering mechanisms in  $\hat{H}_{\text{scatt}}$  and are functionals of the Green's functions. A common graphical representation of the Dyson equation, Eq. (6.18), is



$$(6.20)$$

$$G(\mathbf{k}, E) = G_0(\mathbf{k}, E) + G_0(\mathbf{k}, E) \Sigma(\mathbf{k}, E) G(\mathbf{k}, E),$$

<sup>1</sup>By identifying the bare Green's function  $G_0 = (E - H_0)^{-1}$ , Eq. (6.18) can be expressed in a more common "Dyson form",  $G^{\text{ret}} = G_0 + G_0 \Sigma^{\text{ret}} G^{\text{ret}}$ .

where the thin arrows represent bare or free electron Green's functions,  $G_0$ , and the thick arrows corresponds to dressed or full Green's functions  $G$ . The filled circle represents the self-energy,

$$\Sigma_{\alpha\beta}(\mathbf{q}, E) = \text{---} \circ \text{---}, \quad (6.21)$$

describing the interaction with the scattering potentials. One advantage with self-energies is that they can be expanded into infinite series where each term can be intuitively represented by a Feynman diagram. In the calculations, only one of these terms is included, which corresponds to the self-consistent Born approximation,

$$\begin{aligned} \Sigma_{mn}^{</ret}(\mathbf{k}, E) &= \sum_{\alpha\beta\mathbf{q}} \langle V_{m\alpha}(\mathbf{k}-\mathbf{q}) V_{\beta n}(\mathbf{q}-\mathbf{k}) \rangle_{\text{s.c.}} G_{\alpha\beta}^{</ret}(\mathbf{q}, E) \\ &= \sum_{\mathbf{q}} \text{---} \circ \text{---}, \end{aligned} \quad (6.22)$$

where  $V(\mathbf{q})$  is the scattering potential in momentum space for a static scatterer and the average is over different scattering configurations. Similar expressions for self-energies corresponding to inelastic scattering can be found in Ref. [30]. As for the Green's functions, these self-energies can be related to better-known quantities,

$$\int dE \Sigma_{mm}^{<}(\mathbf{k}, E) \approx i\hbar \sum_{n\mathbf{k}'} f_{n\mathbf{k}'} \Gamma_{n\mathbf{k}' \rightarrow m\mathbf{k}}, \quad (6.23)$$

*i.e.*, the diagonal lesser self-energy can be seen as the scattering into a state. For a detailed discussion on the interpretation of the self-energies, see Chap. 4.4 in Ref. [59]. A similar expression for other self-energies can be found in Ref. [30]. The Keldysh relation and the Dyson equation, together with expressions for the self-energies, such as the Born approximation, constitute a closed set of equations, which can be solved self-consistently using an iterative scheme.

## 6.5 Scattering Averaging

All scattering processes described in Chap. 5 will break the in-plane translation invariance and thus couple states with different wave vector. However, to simplify matters the self-energies are statistically averaged over all possible scattering configurations [64, 65], such that the average of a quantity  $A$  that depends on the spatial location of the impurities  $\{R_i\}$  is [31]

$$\langle A(\{R_i\}) \rangle_{\text{s.c.}} = \prod_i \int_V \frac{dR_i}{V} A(\{R_i\}), \quad (6.24)$$

where any correlations in the impurity positions are neglected. This should be valid in the QCL system of interest here since the in-plane area is large.

Thus, all scattering potentials are treated perturbatively and give a finite lifetime of an electron state with a certain wave vector, which then is reflected in the energy broadening of that state. Since alloy-, ionized impurity- and interface roughness scattering are represented by static potentials, these could in principle be diagonalized and new stationary states would be obtained. The energy broadening in the averaging scheme above would then be reflected by the different energies of the states obtained by diagonalizing the scattering potentials. To the authors knowledge there exist no transport studies without averaged scattering potentials but a study of alloy scattering under strong magnetic fields is presented in Ref. [66]. Also, in Ref. [67], a study of interface roughness scattering with focus on optical linewidth is presented.

## 6.6 Summary

In summary, in the NEGF method, the equations of motion for the quantity  $\langle a_n^\dagger(\mathbf{k}, t_n) a_m(\mathbf{k}, t_m) \rangle$  are solved. Neglecting dynamical effects, *i.e.*, assuming  $t_n = t_m$ , the density matrix approach is obtained and the quantity of interest is  $\langle a_n^\dagger(\mathbf{k}, t) a_m(\mathbf{k}, t) \rangle$ . Going one step further and neglecting coherences one arrives at the rate equation model and only densities are taken into account,  $\langle a_n^\dagger(\mathbf{k}, t) a_n(\mathbf{k}, t) \rangle$ . These methods are suitable for different types of studies, *e.g.*, the numerically demanding NEGF method is probably the method of choice for studying the nature of coherent transport while a fast rate equations implementation can be more efficient when optimizing mid-IR structures or comparing the magnitude of different scattering mechanisms.

# 7

## Screening

The different scattering potentials from the previous chapter will, to different degrees, affect the electron dynamics. Positive potentials will attract electrons and negative will repel electrons. This will give rise to a lowering of the magnitude of the scattering potential and is called *screening*. In this chapter, two different screening models will be derived, first the isotropic screening model, used in the transport calculations in first four papers of this thesis, and discussed in Papers II and V. QCLs are, however, far from isotropic, the thousands of layers in the growth direction can strongly affect the screening, and therefore, a screening model for these multi-subband system is derived in the first section of this chapter and is examined in Paper V.

### 7.1 Induced Charge in Quantum Wells

In this section the amount of induced charge due to a small perturbing potential will be calculated in quantum cascade structures. A first step is to determine the dynamics of the quantity  $\langle \hat{a}_{m,\mathbf{k}-\mathbf{q}}^\dagger \hat{a}_{n,\mathbf{k}} \rangle$ . By combining Eqs. (6.10) and (6.11) the equation of motion is of form,

$$\begin{aligned} \frac{d}{dt} \langle \hat{a}_{m,\mathbf{k}-\mathbf{q}}^\dagger \hat{a}_{n,\mathbf{k}} \rangle &= \frac{i}{\hbar} \langle [\hat{H}, \hat{a}_{m,\mathbf{k}-\mathbf{q}}^\dagger \hat{a}_{n,\mathbf{k}}] \rangle \\ &\quad - \gamma \left( \langle \hat{a}_{m,\mathbf{k}-\mathbf{q}}^\dagger \hat{a}_{n,\mathbf{k}} \rangle - \delta_{\mathbf{q},0} \delta_{m,n} f_{n,\mathbf{k}} \right), \end{aligned} \quad (7.1)$$

where  $\hat{H} = \hat{H}_0 + \hat{H}_{\text{scatt}}$  is the Hamiltonian, and the second row is added to phenomenologically damp the coherences at large times. Later,  $\gamma$  is put to zero. The Hamiltonian can be split up into two parts:  $\hat{H}_0$ , in which the basis is diagonal, and  $\hat{H}_{\text{scatt}}$ , which contains the scattering potential that couples

different momentum states

$$\begin{aligned}\hat{H}_0 &= \sum_{n,\mathbf{k}} E_{n,\mathbf{k}} \hat{a}_{n,\mathbf{k}}^\dagger \hat{a}_{n,\mathbf{k}}, \\ \hat{H}_{\text{scatt}} &= \frac{1}{A} \sum_{n,m} \sum_{\mathbf{k},\mathbf{q} \neq 0} V_{mn}(\mathbf{q}, t) \hat{a}_{m,\mathbf{k}+\mathbf{q}}^\dagger \hat{a}_{n,\mathbf{k}},\end{aligned}\quad (7.2)$$

where  $V_{mn}(\mathbf{q}, t)$  is related to the scattering potential via,

$$V(\vec{r}, t) = \frac{1}{A} \sum_{\mathbf{q}} \sum_{m,n} V_{mn}(\mathbf{q}, t) \psi_m^*(z) \psi_n(z) e^{i\mathbf{q}\cdot\mathbf{r}}. \quad (7.3)$$

Note that the potential is defined in units of electron energy, *i.e.*, the electron charge times the electrostatic potential. Also, the charge density is given by

$$\rho(\vec{r}) = 2 \frac{e}{A} \sum_{n,n'} \sum_{\mathbf{k},\mathbf{q}} \psi_n^*(z) \psi_{n'}(z) e^{i\mathbf{q}\cdot\mathbf{r}} \langle \hat{a}_{n,\mathbf{k}-\mathbf{q}}^\dagger \hat{a}_{n',\mathbf{k}} \rangle, \quad (7.4)$$

where the factor 2 in front is due to the spin degeneracy.

A Fourier transformation in time of Eq. (7.1) will result in the transformations  $d_t \rightarrow -i\omega$  and  $1 \rightarrow 2\pi\delta(\omega)$ . To linear order in the scattering potential, *i.e.*,  $\langle \hat{a}_i^\dagger \hat{a}_j \rangle = f_i \delta_{i,j} + O\{V\}$ , the result is

$$\begin{aligned}\langle \hat{a}_{m,\mathbf{k}-\mathbf{q}}^\dagger \hat{a}_{n,\mathbf{k}} \rangle_\omega &= 2\pi \delta_{\mathbf{q},0} \delta_{m,n} f_{n,\mathbf{k}} \\ &+ \frac{1}{A} \frac{f_{m,\mathbf{k}-\mathbf{q}} - f_{n,\mathbf{k}}}{E_{m,\mathbf{k}-\mathbf{q}} - E_{n,\mathbf{k}} + \hbar\omega + i\hbar\gamma} V_{mn}(\mathbf{q}, \omega) + O\{V^2\}.\end{aligned}\quad (7.5)$$

By Eq. (7.4), the induced charge density due to the potential, is given by

$$\rho_{mn}^{\text{ind}}(\mathbf{q}, \omega) = 2 \frac{e}{A} \sum_{\mathbf{k}} \frac{f_{m,\mathbf{k}-\mathbf{q}} - f_{n,\mathbf{k}}}{E_{m,\mathbf{k}-\mathbf{q}} - E_{n,\mathbf{k}} + \hbar\omega + i\hbar\gamma} V_{mn}(\mathbf{q}, \omega). \quad (7.6)$$

The proportionality constant between the induced charge and the potential is called the *polarizability* or polarization function,

$$\Pi_{nm}(\mathbf{q}, \omega) = \lim_{\gamma \rightarrow 0} \frac{2}{A} \sum_{\mathbf{k}} \frac{f_{m,\mathbf{k}+\mathbf{q}} - f_{n,\mathbf{k}}}{E_{m,\mathbf{k}+\mathbf{q}} - E_{n,\mathbf{k}} - \hbar\omega - i\hbar\gamma}. \quad (7.7)$$

This form of the polarizability is called the *Random Phase Approximation* (RPA) [68], and can be seen as a time dependent Hartree approximation for screening. Worth noting is that in the static case ( $\omega = 0$ ), the polarizability is the occupation difference divided by the energy difference, which at equilibrium always is negative. As  $e < 0$ , Eq. (7.6) shows that a positive electron potential

will, quite intuitively, accumulate positive charge, or repel electrons. In the dynamical situation ( $\omega \neq 0$ ), or in non-equilibrium systems, this will no longer be the case. Evaluation of the polarizability for realistic structures is discussed in App. A.

To summarize, in the presence of a scattering potential the electrons will not only interact with the potential, but also the induced charge. The next step is to calculate the interaction with the induced charge, which also will be screened.

## 7.2 Isotropic Screening

Calculating the screened potential in realistic QCLs under operational conditions is a complex task that has to be solved numerically. A simpler situation, an ionized dopant screened by an isotropic electron gas at thermal equilibrium, can be calculated analytically.

The effective, or total, scattering potential is the sum of the potential from the bare impurity and the potential from the induced charge,

$$V^{\text{eff}}(\vec{r}) = V^{\text{imp}}(\vec{r}) + V^{\text{ind}}(\vec{r}). \quad (7.8)$$

In the mean-field approximation, the induced potential is governed by the Poisson equation,

$$\nabla^2 V^{\text{ind}}(\vec{r}) = -\frac{e\bar{\rho}^{\text{ind}}(\vec{r})}{\varepsilon_r \varepsilon_0}, \quad (7.9)$$

which can easily be solved in momentum space,

$$V^{\text{ind}}(\vec{q}) = \frac{e\rho^{\text{ind}}(\vec{q})}{\varepsilon_r \varepsilon_0 |\vec{q}|^2} = V^{\text{ee}}(\vec{q})\Pi(\vec{q})V^{\text{eff}}(\vec{q}), \quad (7.10)$$

where  $V^{\text{ee}}(\vec{q}) = e^2/\varepsilon_r \varepsilon_0 |\vec{q}|^2$  is the unscreened electron-electron matrix element in 3 dimensions, and the induced charge is  $\Pi(\vec{q})V^{\text{eff}}(\vec{q})$ . Note that the effective potential is giving rise to the charge, and not only in the impurity potential. This choice gives a self-consistent effective potential, which now can be expressed by

$$V^{\text{eff}}(\vec{q}) = \frac{V^{\text{imp}}(\vec{q})}{1 - V^{\text{ee}}(\vec{q})\Pi(\vec{q})}. \quad (7.11)$$

In this isotropic system, the polarizability has a similar form as in previous section, however without the subband-index. The assumption of static

screening and long wavelength results in

$$\begin{aligned}\Pi(\vec{q}) &= \frac{2}{V} \sum_{\vec{k}} \frac{f_{\vec{k}-\vec{q}} - f_{\vec{k}}}{E_{\vec{k}-\vec{q}} - E_{\vec{k}}} \approx \frac{2}{V} \sum_{\vec{k}} \frac{-\vec{q} \cdot \nabla_{\vec{k}} f_{\vec{k}}}{-\vec{q} \cdot \nabla_{\vec{k}} E_{\vec{k}}} \\ &= \frac{2}{V} \sum_{\vec{k}} \frac{-\vec{q} \cdot \nabla_{\vec{k}} E_{\vec{k}} \frac{\partial f_{\vec{k}}}{\partial \mu}}{-\vec{q} \cdot \nabla_{\vec{k}} E_{\vec{k}}} = \frac{\partial}{\partial \mu} \frac{2}{V} \sum_{\vec{k}} f_{\vec{k}} = \frac{\partial n}{\partial \mu}.\end{aligned}\quad (7.12)$$

With the inverse screening length defined as

$$\lambda = \sqrt{\frac{e^2}{\epsilon_r \epsilon_0} \frac{\partial n}{\partial \mu}}, \quad (7.13)$$

the effective potential from a point charge with charge  $e$  located at the origin becomes,

$$V^{\text{eff}}(\vec{r}) = \frac{e^2}{4\pi\epsilon_r\epsilon_0|\vec{r}|} e^{-\lambda|\vec{r}|} = V^{\text{imp}}(\vec{r}) e^{-\lambda|\vec{r}|} \quad (7.14)$$

which clearly illustrates the role of the inverse screening length, namely that the Coulomb potential is exponentially suppressed at distances corresponding to the screening length.

The partial derivative in the expression for the screening length can be evaluated in two limits: First, the non-degenerate, high temperature limit, where the electron distribution can be approximated by a Boltzmann distribution,

$$\frac{\partial n}{\partial \mu} = \frac{\partial}{\partial \mu} \frac{2}{V} \sum_{\vec{k}} f_{\vec{k}}^{FD} \approx \frac{\partial}{\partial \mu} \frac{2}{V} \sum_{\vec{k}} e^{-(E_{\vec{k}} - \mu)/k_B T} = \frac{n}{k_B T}, \quad (7.15)$$

which is called Debye screening. The second case is the degenerate, low temperature, limit called Thomas-Fermi screening where the distribution function is approximated with a step function,  $f_{\vec{k}}^{FD} = \theta(\mu - E_{\vec{k}})$ . The resulting charge accumulation is

$$\frac{\partial n}{\partial \mu} \approx \frac{m}{\pi^{4/3} \hbar^2} (3n)^{1/3}, \quad (7.16)$$

valid at very low temperatures, or high electron concentrations.

One central result in Paper V is that when the screening length is of the order of the period of the laser structure or longer, all electrons contribute to screening and the isotropic screening model described above gives excellent agreement with the full RPA model with non-equilibrium distributions.

### 7.3 Screened Electron-Electron Interaction

In the first section of this chapter the polarizability for quantum cascade structures was derived. The next step is to calculate the screened impurity potentials

in this anisotropic subband system. One approach, as outlined below and used in Paper V, is to first calculate the screened electron-electron interaction and then determine the screened scattering potentials.

The bare, or unscreened, electron-electron interaction is

$$V(\vec{r}_1, \vec{r}_2) = \frac{e^2}{4\pi\epsilon_r\epsilon_0|\vec{r}_1 - \vec{r}_2|}, \quad (7.17)$$

or, in the layered structures of interest here, its matrix elements are given by

$$V_{ijkl}(q) = \frac{e^2}{2A\epsilon_0\epsilon_r} \frac{F_{ijkl}(q)}{q}, \quad (7.18)$$

where the form factors are

$$F_{ijkl}(q) = \int dz \int dz' \psi_i^*(z) \psi_j(z) e^{-q|z-z'|} \psi_k^*(z') \psi_l(z'). \quad (7.19)$$

Calculating these matrix elements is computationally demanding and numerical efficient schemes are presented in App. B.

The screened interaction matrix elements,  $W_{ijkl}(q, \omega)$ , can be evaluated via the infinite sum

$$W = V + V\Pi V + V\Pi V\Pi V + \dots, \quad (7.20)$$

where the subband indices and the wave vector and frequency dependence have been omitted for simplicity. The first term on the right side represents the direct interaction, the second term interaction with the induced charge density, the third term represents interaction with the induced charge density by the induced charge density, and so on. Along the lines of previous section, this expression can be rewritten to

$$W = V + V\Pi(V + V\Pi V + \dots) = V + V\Pi W, \quad (7.21)$$

which is known as the Dyson equation. Including indices, wave vector and frequency, the equation is

$$W_{ijkl}(q, \omega) = V_{ijkl}(q) + \sum_{mn} V_{ijnm}(q) \Pi_{mn}(q, \omega) W_{mnkl}(q, \omega), \quad (7.22)$$

which is studied in detail for quantum cascade structures in Paper V. These equations have a common graphical representation with Feynman diagrams,



$$\begin{aligned}
\text{---} &= \text{---} + \text{---} \text{---} + \text{---} \text{---} \text{---} + \dots \\
&= \text{---} + \text{---} \text{---} \times \left[ \text{---} + \text{---} \text{---} + \dots \right] \\
&= \text{---} + \text{---} \text{---},
\end{aligned} \tag{7.23}$$

which is identical to Eq. (7.22). The double and single wavy lines corresponds to bare and screened electron-electron interaction respectively, and the ‘‘bubble’’ corresponds to the polarization,

$$V_{ijkl}(\mathbf{q}) = \begin{array}{c} j \\ \swarrow \quad \searrow \\ \text{---} \\ \swarrow \quad \searrow \\ i \quad \quad k \end{array}, \quad \Pi_{ijkl}(\mathbf{q}, E) = \begin{array}{c} G_{lj}(\mathbf{k}, E') \\ \circlearrowleft \\ G_{ik}(\mathbf{q} + \mathbf{k}, E + E') \end{array}. \tag{7.24}$$

This diagrammatic approach gives a simple interpretation of the polarizability, namely the creation of an electron-hole pair, where a Green’s function line with arrow in the opposite direction corresponds to a hole. Also, this diagrammatic form of the polarizability suggests the expression (Eq. (18.9) in Ref. [31] Fourier transformed),

$$\Pi_{ijkl}(\mathbf{q}, E) \approx -2i \sum_{\mathbf{k}} \int \frac{dE'}{2\pi} G_{ik}(\mathbf{k} + \mathbf{q}, E' + E) G_{lj}(\mathbf{k}, E'). \tag{7.25}$$

Time ordering, together with a simplified form of the Green’s functions [69]

$$G_{ij}^{\text{ret/adv}}(\mathbf{k}, E) \approx \delta_{ij} \frac{1}{E - E_{i,\mathbf{k}} \pm i\Gamma_i/2}, \tag{7.26}$$

yields (Eq. (18.18) in Ref. [31] Fourier transformed at steady state)

$$\begin{aligned}
\Pi_{ijkl}^{\text{ret}}(\mathbf{q}, E) &\approx -2i \sum_{\mathbf{k}} \int \frac{dE'}{2\pi} G_{ik}^{\text{ret}}(\mathbf{k} + \mathbf{q}, E' + E) G_{jl}^{\text{adv}}(\mathbf{k}, E') [f_{j,\mathbf{k}} - f_{i,\mathbf{k}+\mathbf{q}}] \\
&= -2i \delta_{ik} \delta_{jl} \sum_{\mathbf{k}} \int \frac{dE'}{2\pi} \frac{f_{j,\mathbf{k}} - f_{i,\mathbf{k}+\mathbf{q}}}{(E' + E - E_{i,\mathbf{k}+\mathbf{q}} + i\Gamma_i/2)(E' - E_{j,\mathbf{k}} - i\Gamma_j/2)} \\
&= 2\delta_{ik} \delta_{jl} \sum_{\mathbf{k}} \frac{f_{j,\mathbf{k}} - f_{i,\mathbf{k}+\mathbf{q}}}{E_{j,\mathbf{k}} + E - E_{i,\mathbf{k}+\mathbf{q}} + i(\Gamma_j + \Gamma_i)/2} \\
&= 2\delta_{ik} \delta_{jl} \sum_{\mathbf{k}} \frac{f_{i,\mathbf{k}+\mathbf{q}} - f_{j,\mathbf{k}}}{E_{i,\mathbf{k}+\mathbf{q}} - E_{j,\mathbf{k}} - E - i(\Gamma_j + \Gamma_i)/2},
\end{aligned} \tag{7.27}$$

which indeed is similar to Eq. (7.7) derived earlier in this section. This derivation of the polarizability shed light on two things. First, the reason for that the polarizability only has two indices, and not four like the electron-electron interaction matrix element is that the constituent Greens functions are assumed to be diagonal. Secondly, the  $\gamma$  in Eq. (7.7) (and the  $\delta$  in Eq. (6) in Paper V) reflect the spectral width of the Green's functions. However, one should note that approximating the  $\gamma$  in Eq. (7.7) by the average spectral width of the Green's functions,  $(\Gamma_j + \Gamma_i)/2$  as suggested above, is a strong over-estimate [70], and a more detailed calculation is necessary. A more detailed self-consistent calculation would yield a finite  $\gamma$  when calculating the polarizability. This is expected to decrease the polarizability and therefore diminish the screening and increase scattering.

Once screened electron-electron interaction matrix elements are obtained from solving Eq. (7.22) by inversion, the screened matrix element can be obtained by direct multiplication,

$$\begin{aligned}
&\bullet \blacktriangleleft \star = \bullet \blacktriangleleft \star + \bullet \text{---} \text{---} \text{---} \star + \bullet \text{---} \text{---} \text{---} \text{---} \star + \bullet \text{---} \text{---} \text{---} \text{---} \text{---} \star + \dots \\
&= \bullet \blacktriangleleft \star + \left[ \bullet \text{---} \text{---} \text{---} + \bullet \text{---} \text{---} \text{---} \text{---} + \dots \right] \times \bullet \text{---} \text{---} \text{---} \star \\
&= \bullet \blacktriangleleft \star + \bullet \text{---} \text{---} \text{---} \star,
\end{aligned} \tag{7.28}$$

where the screened impurity scattering matrix element is represented by

$$W_{\alpha\beta}^{\text{imp}}(\mathbf{q}, \omega) = \begin{matrix} \beta \\ \blacktriangleright \\ \bullet \\ \blacktriangleleft \\ \alpha \end{matrix} = \begin{matrix} \bullet \\ \text{---} \text{---} \text{---} \\ \blacktriangleleft \end{matrix} = \begin{matrix} \bullet \\ \text{---} \text{---} \text{---} \\ \star \end{matrix}. \tag{7.29}$$

The approach outlined above was used in Paper V. An alternative approach would be to group the diagrams to form a Dyson equation for the impurity matrix elements. This way, the screened electron-electron matrix elements do not have to be calculated explicitly [71],

$$\begin{aligned}
 \bullet &= \blacktriangleleft = \star = \bullet \blacktriangleleft \star + \bullet \text{---} \bullet \text{---} \bullet \text{---} \bullet \text{---} \bullet \text{---} \star + \dots \\
 &= \bullet \blacktriangleleft \star + \bullet \text{---} \bullet \text{---} \bullet \text{---} \bullet \text{---} \star \left[ \bullet \blacktriangleleft \star + \bullet \text{---} \bullet \text{---} \bullet \text{---} \bullet \text{---} \star + \dots \right] \\
 &= \bullet \blacktriangleleft \star + \bullet \text{---} \bullet \text{---} \bullet \text{---} \star.
 \end{aligned}$$

(7.30)

# 8

## Light Matter Interaction

The macroscopic Maxwell equations, governing the electromagnetic field in the presence of materials,

$$\begin{aligned}\nabla \cdot \vec{D} &= \rho & \nabla \times \vec{E} &= -\frac{\partial \vec{B}}{\partial t} \\ \nabla \cdot \vec{B} &= 0 & \nabla \times \vec{H} &= \frac{\partial \vec{D}}{\partial t} + \vec{j},\end{aligned}\tag{8.1}$$

can be solved together with the constitutive relations, describing the material properties,

$$\begin{aligned}\vec{D} &= \varepsilon_0 \varepsilon_{\text{tot}} \vec{E} = \varepsilon_0 \varepsilon_r \vec{E} + \vec{P} = \varepsilon_0 \varepsilon_r (1 + \chi^{\text{rel}}) \vec{E}, \\ \vec{H} &= \frac{1}{\mu_0 \mu_r} \vec{B} = \frac{1}{\mu_0} \vec{B} - \vec{M},\end{aligned}\tag{8.2}$$

where  $\varepsilon_{\text{tot}}$  is the total relative dielectric constant or permittivity and  $\varepsilon_r$  is the relative dielectric constant of the background material, in most cases bulk GaAs och InP, and  $\chi^{\text{rel}}$  is the susceptibility due to polarization of the electrons in the subband system of the QCL. The background dielectric constant is related to the index of refraction,  $n$ , via

$$n^2 = \varepsilon_r,\tag{8.3}$$

assuming a non-magnetic material ( $\mu_r = 1$ ). The semiconductor materials used for QCLs will throughout this treatment be assumed to be non-magnetic.

The left two equations in Eq. (8.1) only give rise to static fields and are therefore not considered here. Thus, Eq. (8.1) becomes

$$\begin{aligned}\nabla \times \vec{E} &= -\frac{\partial \vec{B}}{\partial t}, \\ \nabla \times \vec{B} &= \varepsilon_0 \varepsilon_r \mu_0 \frac{\partial \vec{E}}{\partial t} + \mu_0 \left( \frac{\partial \vec{P}}{\partial t} + \vec{j} \right),\end{aligned}\tag{8.4}$$

where the terms in the parenthesis are the source terms. By taking the curl of the first equation, the wave equation for the electric field is obtained<sup>1</sup>

$$\varepsilon_0 \varepsilon_r \mu_0 \frac{\partial^2 \vec{E}}{\partial t^2} - \nabla^2 \vec{E} = -\mu_0 \left( \frac{\partial^2 \vec{P}}{\partial t^2} + \frac{\partial \vec{j}}{\partial t} \right). \quad (8.5)$$

Using a plane wave traveling in the  $y$ -direction and polarized in the  $z$ -direction as ansatz,

$$\vec{E}(\vec{r}, t) = \Re\{E(y)\vec{e}_z e^{i(ky - \omega t)}\}, \quad (8.6)$$

together with the relations  $\vec{P} = \chi^{\text{rel}} \varepsilon_0 \varepsilon_r \vec{E}$  and  $\vec{j} = \sigma \vec{E}$ , where  $\sigma$  is the conductivity, Eq (8.5) becomes

$$2ik \frac{dE(y)}{dy} + (\omega^2 \varepsilon_0 \varepsilon_r \mu_0 - k^2)E(y) = \mu_0 (-\omega^2 \chi^{\text{rel}}(\omega) \varepsilon_0 \varepsilon_r E(y) - i\omega \sigma(\omega) E(y)). \quad (8.7)$$

Here, a short wavelength compared to the length scale of the amplification of the electric field has been assumed, so that the second order spatial derivative of  $E(y)$  can be neglected<sup>2</sup>. As  $\omega^2 \varepsilon_r \varepsilon_0 \mu_0 = k^2$ , the equation above can be simplified to

$$\frac{dE(y)}{dy} = \left( i \frac{\omega \sqrt{\varepsilon_r}}{2c} \chi(\omega) - \frac{1}{2c \varepsilon_0 \sqrt{\varepsilon_r}} \sigma(\omega) \right) E(y), \quad (8.8)$$

where  $c = n\omega/k$  is the speed of light in vacuum. The gain of the material,  $g(\omega)$ , can be defined as<sup>3</sup>

$$\frac{d|E(y)|}{dy} = \frac{g}{2}|E(y)|. \quad (8.9)$$

Thus, the gain can be calculated with Eq. (8.8) by dividing the electric field into amplitude and phase,  $E(y) = |E(y)|e^{i\phi(y)}$ . The gain is then

$$g(\omega) = -\frac{\omega \sqrt{\varepsilon_r}}{c} \Im\{\chi(\omega)\} - \frac{1}{c \varepsilon_0 \sqrt{\varepsilon_r}} \Re\{\sigma(\omega)\}, \quad (8.10)$$

which has been the starting point when deriving the spatial resolved gain in Paper I.

According to Eq. (8.10), electromagnetic fields can be affected by currents, via the conductivity, and by polarizations, via the susceptibility. At lower frequencies than THz, often currents are the source of radiation such as in

<sup>1</sup> $\nabla \times \nabla \times \vec{E} = \nabla(\nabla \cdot \vec{E}) - \nabla^2 \vec{E}$  and  $\nabla \cdot \vec{E} = 0$  as the electric field is polarized perpendicular to the direction of propagation for a plane wave.

<sup>2</sup>Typical gain in THz lasers is  $\sim 20 \text{ cm}^{-1}$ , which is much longer length scale than wave vector in the medium,  $k \approx 2\pi/(200 \mu\text{m}/n) \approx 1000 \text{ cm}^{-1}$

<sup>3</sup>The factor 1/2 comes from that the gain usually is defined for the intensity  $I \propto E^2$

antennas connected to some transistor or other electronics. At frequencies higher than THz, the tradition is often that polarizations are giving rise to the radiating fields. The two contributions come from the popular division of the charge into bound charges, giving rise to polarizations, and free charges that can cause currents, see, *e.g.*, Sect. 6.6 in Ref. [72]. In most systems this division is clear, while the QCL is a system between the two regimes. The same electrons that emit light are giving rise to the electrical current suggesting that they are free, while the light is emitted in transitions between spatially localized quantum states suggesting the polarization description.

## 8.1 Microscopic Approach

In the previous section, the way was described in which electromagnetic fields interact with a material from a macroscopic point of view. Here, instead a more microscopic approach is presented. The mechanisms with which electrons interact with electromagnetic radiation are central when analyzing laser materials. Either the electromagnetic field is being amplified by the electrons, known as gain, or the radiation is being absorbed. The Hamiltonian for an electron in the presence of an electromagnetic field is

$$\hat{H} = \frac{1}{2m} \left( \hat{\vec{p}} - e\vec{A}(\vec{r}, t) \right)^2 + e\phi(\vec{r}, t), \quad (8.11)$$

where  $\vec{A}$  and  $\phi$  are the electromagnetic vector and scalar potential, respectively, related to the electromagnetic field by

$$\vec{E} = -\nabla\phi - \frac{\partial\vec{A}}{\partial t}, \quad \vec{B} = \nabla \times \vec{A}. \quad (8.12)$$

If the  $A^2$ -term is neglected and  $\hat{\vec{p}}$  and  $\vec{A}$  are assumed to commute, the perturbing term in the Hamiltonian due to the radiation field is

$$\hat{H}_{\text{em}} \approx \frac{e}{m} \hat{\vec{p}} \cdot \vec{A}(\vec{r}, t). \quad (8.13)$$

Using Fermi's Golden Rule [73], the rate of optical transitions from state  $u$  to  $l$  (upper and lower laser state) is

$$\Gamma_{u \rightarrow l}^{\text{em}} = \frac{2\pi}{\hbar} |\langle \psi_l | \hat{H}_{\text{em}} | \psi_u \rangle|^2 \delta(E_u - E_l - \hbar\omega) \quad (8.14)$$

where  $\omega$  is the angular frequency of the incoming electromagnetic radiation.

The gain from two states,  $u$  and  $l$  where  $E_u > E_l$ , can then be defined as the number of photons generated minus the number absorbed per volume divided

by the incoming photon flux,

$$\begin{aligned} g(\omega) &= \frac{\hbar\omega}{V} \frac{\Gamma_{u \rightarrow l}^{\text{stim. em.}} - \Gamma_{l \rightarrow u}^{\text{stim. abs.}}}{\text{Photon flux per area}} \\ &= \frac{\pi\omega |ez_{ul}|^2}{\sqrt{\epsilon_r c \epsilon_0} V} \delta(E_u - E_l - \hbar\omega) (f_u - f_l), \end{aligned} \quad (8.15)$$

where  $z_{ul} = \langle \psi_u | z | \psi_l \rangle$ . Worth noticing here is that the only way to achieve positive gain is through population inversion, *i.e.*,  $f_u > f_l$ . However, a more detailed derivation of the material gain will show that a positive gain can be observed without inversion [74].

According to Eq. (8.15), non-zero gain or absorption only occurs at discrete energies. This unphysical result can be circumvented by replacing the  $\delta(E)$ -function with a Lorentzian,

$$\delta(E - E_0) \longrightarrow \frac{1}{\pi} \frac{\Gamma/2}{(E - E_0)^2 + (\Gamma/2)^2}, \quad (8.16)$$

where  $\Gamma$  is the full width at half maximum of the peak.  $\Gamma$  is usually chosen to be the sum of the lifetime induced energetic widths of the two corresponding states. This approximation works well for mid-IR devices, while for THz devices, correlations in the scattering environment of the two states can be of importance [69], see also Papers II, IV and V. This correlation in the scattering potential of the two states causes the gain/absorption peak to be narrower than the sum of the scattering induced energetic width of the two respective states. Taking this effect into account is crucial for THz devices where the energy separation of the two lasing states is comparable to their widths.

## 8.2 $\vec{p} \cdot \vec{A}$ vs. $\vec{r} \cdot \vec{E}$

From the definition of the scalar and vector potential, Eq. (8.12), it is clear that any change in the vector and scalar potential that can be expressed by a function  $\Lambda(\vec{r}, t)$  via

$$\vec{A}' = \vec{A} + \nabla\Lambda, \quad \Phi' = \Phi - \frac{\partial\Lambda}{\partial t}, \quad (8.17)$$

will not change the physical electric and magnetic field. This invariance in the potentials is called *gauge invariance*, and similarly, the transformation above is called *gauge transformation*. Typically, two difference gauges are used. First, the Lorenz gauge or velocity gauge defined by

$$\nabla \cdot \vec{A} + \frac{1}{c^2} \frac{\partial\Phi}{\partial t} = 0, \quad (8.18)$$

and secondly, the Coulomb gauge, or radiation-, or length-, or transverse gauge is defined by

$$\nabla \cdot \vec{A} = 0. \quad (8.19)$$

The electromagnetic field present in the QCL due to the laser light can be written as

$$\vec{E}(\vec{r}, t) = E_0 \vec{e}_z e^{i(ky - \omega t)}, \quad \vec{B}(\vec{r}, t) = \frac{k}{\omega} E_0 \vec{e}_x e^{i(ky - \omega t)}, \quad (8.20)$$

which becomes

$$\vec{A}(\vec{r}, t) = -\frac{k}{\omega} E_0 z \vec{e}_y e^{i(ky - \omega t)}, \quad \Phi(\vec{r}, t) = -E_0 z e^{i(ky - \omega t)}, \quad (8.21)$$

in Lorenz gauge and

$$\vec{A}(\vec{r}, t) = \frac{E_0}{i\omega} \vec{e}_z e^{i(ky - \omega t)}, \quad \Phi(\vec{r}, t) = 0. \quad (8.22)$$

and Coulomb gauge. To simplify matters, the long wavelength approximation is often employed in Lorenz gauge. As the typical wavelength for a THz laser is  $\sim 30 \mu\text{m}$  and the size of the wavefunctions in the  $z$  direction  $\sim 30 \text{ nm}$ ,  $kz = 2\pi z/\lambda \ll 1$  in the expression for the vector potential and is therefore neglected. This results in the simple rule that in Lorenz gauge the laser field couples to the electron via the position and in Coulomb gauge via the momentum.

The two different couplings of the electron Hamiltonian to the electromagnetic field are

$$\begin{aligned} \hat{H}_{\text{em}}^{\text{Lorenz}} &= e\Phi(\vec{r}, t) = -eE_0 z e^{i(ky - \omega t)}, \\ \hat{H}_{\text{em}}^{\text{Coul.}} &= \frac{e}{m} \hat{p} \cdot \vec{A}(\vec{r}, t) = \frac{e}{m} \hat{p}_z \frac{E_0}{i\omega} e^{i(ky - \omega t)}. \end{aligned} \quad (8.23)$$

Although quantum mechanics can be proven to be gauge invariant<sup>4</sup>, the two different couplings will in simplified situations give different results [75, 76].

If only two states are considered,  $|u\rangle$  and  $|l\rangle$ , which are eigenstates of the Hamiltonian without the applied electromagnetic field, the momentum matrix element can be rewritten,

$$p_{ul} = m \frac{dr_{ul}}{dt} = \frac{im}{\hbar} [r, H]_{ul} = -\frac{im}{\hbar} \Delta E_{ul} r_{ul}, \quad (8.24)$$

where  $\Delta E_{ul} = E_u - E_l$ . This leads to a simple ratio between the interaction Hamiltonians for the two gauges,

$$\frac{H_{\text{em}}^{\text{Lorenz}}}{H_{\text{em}}^{\text{Coul.}}} = \frac{\hbar\omega}{\Delta E_{ul}}. \quad (8.25)$$

<sup>4</sup>The Hamiltonian in Eq. (8.11) is invariant under the transformation Eq. (8.17) together with the unitary transformation  $\psi'(\vec{r}, t) = e^{i\Lambda(\vec{r}, t)} \psi(\vec{r}, t)$



For a simple model, with only resonant interaction, the two couplings are identical. However, in THz QCLs, where the width can be a substantial fraction of the central frequency, this difference can result in a quite large difference in gain. Also, as low frequencies often are desired, waveguides can be designed to support radiation on the low-frequency side of the gain peak where the Coulomb gauge is expected to give higher gain. *E.g.*, in Paper II, the laser emitted at 7.9 meV while the peak gain occurred at 9 meV.

Part of the reason for this discrepancy between the two gauges is that in the example above and in most calculations, truncated Hilbert space are used. If broadening occurs, the electromagnetic field induces transitions between *all* possible states in the system, which must be taken into account. By an argument presented in Ref. [77], the position matrix elements are all bound by the size of the system, while the momentum matrix element  $p_{\alpha\beta} \propto \Delta E_{\alpha\beta} z_{\alpha\beta}$  increase with energy difference. As the Hilbert space often is truncated at a certain energy, the error is larger for the momentum matrix elements and hence a larger error is expected in the Coulomb gauge.

A second inconsistency in finite Hilbert spaces is the canonical commutation relation,  $[z, p] = i\hbar$ , used in the derivation of gauge invariance, is not valid [77]. If all states are equally populated, the density matrix is proportional to the identity matrix,  $\rho = I/N$ , where  $N$  is the number of states in the considered system. The expectation value of the operation  $[z, p]$  is then both  $i\hbar$  and 0. By the use of Eq. (6.11)

$$\begin{aligned} \langle [z, p] \rangle &= \text{Tr}\{[z, p]\rho\} = \frac{i\hbar}{N} \text{Tr}\{I\} = i\hbar, \\ \langle [z, p] \rangle &= \text{Tr}\{(zp - pz)\rho\} = \frac{1}{N} \text{Tr}\{zp - pz\} = 0, \end{aligned} \tag{8.26}$$

where in the second row, the cyclic property of the trace has been used. Hence,  $[z, p] \neq i\hbar$  in finite Hilbert spaces. As the proof for gauge invariance is based on the validity of this commutation relation, numerical calculations in which finite Hilbert spaces are used, are not necessarily gauge invariant.

A similar problem occurs when calculating the gain. From Eq. (8.10) it can be seen that the gain can either be calculated from the susceptibility or the conductivity. The susceptibility is obtained by calculating the polarization, *i.e.*, the change in position,  $\delta z$ , induced by the electromagnetic field. Similarly, the conductivity is obtained by the change in current,  $\delta J$ , which is proportional to the change in momentum,  $\delta p$  [74]. As for the coupling of the electromagnetic field to the electron, whether  $\delta z$  or  $\delta p$  is chosen the result differs by a factor of  $\hbar\omega/\Delta E_{\text{ul}}$ . The results are summarized in Tab. 8.1.

	$z \cdot F$	$p \cdot A$
$\chi \rightarrow \delta z$	$g \propto \omega$	$g \propto \Delta E$
$\sigma \rightarrow \delta J \propto \delta p_z$	$g \propto \Delta E$	$g \propto \frac{(\Delta E)^2}{\omega}$

Table 8.1: Different couplings of the electromagnetic field to the motion on the electrons give different expressions for the gain when energetic broadening of the states is considered. Also, defining the gain from the response in different observables gives different results.

### 8.3 Spectral Broadening and Correlation Effects

With a simple Lorentzian model for the gain spectra, the peak gain is inversely proportional to the linewidth and proportional to the inverted population. The linewidth of the transition reflects the energetic width, or uncertainty, of the two lasing states. This width can be estimated by the time-energy uncertainty,

$$\Delta E \cdot \Delta t \approx \hbar, \quad (8.27)$$

where  $\Delta t$  corresponds to the lifetime of the electron in the lasing states.

This energetic broadening of the states gives a finite width of the optical transition. A first estimate is that the optical linewidth is the sum of the energetic width of the two corresponding states. This is an excellent estimate for mid-IR lasers, but strongly over-estimates the optical linewidth for THz QCLs due to neglecting the *correlation effects* [69, 78].

If the same scattering mechanism is causing the width of the two lasing states, the optical linewidth can be smaller than the sum of the widths of the respective states. These correlations in the scattering environment are difficult to quantify, but a simple approach results in a spectral linewidth that is a measure of the square of the difference in the scattering matrix element, and not the sum of squares, see, *e.g.*, Refs. [69, 79], Paper V or Fig. 3 in Paper IV,

$$\begin{aligned} \Gamma_{\text{no.corr}}(\mathbf{q}) &\propto \langle V_u^2(\mathbf{q}) + V_l^2(\mathbf{q}) \rangle_{\text{s.c.}}, \\ \Gamma_{\text{simp.corr}}(\mathbf{q}) &\propto \langle |V_u(\mathbf{q}) - V_l(\mathbf{q})|^2 \rangle_{\text{s.c.}}. \end{aligned} \quad (8.28)$$

The correlation effects in these systems are well explained in Ref. [78]. The light interacts with a polarization between the upper and lower laser level, which means that the electron is in a superposition between the upper and lower laser level at a certain wave vector,  $\alpha|u, \mathbf{k}\rangle + \beta|l, \mathbf{k}\rangle$ . If the intraband scattering matrix elements are identical for the two laser levels a scattering event does not destroy the coherences and the resulting state after the scattering occurred is  $\alpha|u, \mathbf{k}'\rangle + \beta|l, \mathbf{k}'\rangle$ . In these intersubband devices the curvature of the subbands are approximately the same and, hence, the energy difference

between the upper and lower subband is independent of wave vector. Since a scattering mechanism with identical matrix element for both laser levels does not affect the polarization, this does not give rise to spectral broadening. By this argument the spectral broadening should be better described by the difference in scattering environments, as used in Paper V.

At higher temperatures the width is expected to increase due to more scattering, which is caused by both more phonons and less screening. In Paper II a calculation is presented that shows that the linewidth of the gain transition is expected to increase with temperature and approximately follow the impurity scattering strength, at least for low temperatures.

Another aspect regarding correlation effects is the discussion on scattering averaging in Chap. 6. In standard laser theory, see, *e.g.*, Sect. 2.5 in Ref. [80], the contributions to the optical linewidth is divided into *homogenous* and *inhomogeneous* parts. In ordinary gas or solid-state lasers each lasing atom is clearly spatially isolated, and will therefore have an intrinsic linewidth mainly due to lifetime broadening. This is homogenous broadening. Especially in solid-state lasers, each lasing atom will be influenced by a different random crystal strain field that will shift the lasing frequency slightly. Adding the spectra of all lasing atoms with their respective randomly shifted lasing frequency will give a inhomogeneously broadened spectra.

If different wave vector states in QCLs correspond to different atoms in standard lasers no inhomogeneous linewidth is present in our model. This is however due to the scattering averaging, where all scattering mechanisms are assumed to give lifetime broadening, while preserving wave vector as a good quantum number, instead of shifting the energy between two lasing states. However, as described in Chap. 6, many scattering potentials are static and in a more detailed calculation the lasing should occur between states obtain by diagonalizing the scattering potential. This would result in inhomogeneous broadening instead, and the inclusion of correlation effect on a more intuitive level [67].

## 8.4 Dispersive Gain

The underlying approximation by assuming Lorentzian lineshape in Eq. (8.16) is that the spectral function,  $A_\alpha(\mathbf{k}, E)$ , similar to a density of states for a single state, is Lorentzian in shape,

$$A_\alpha(\mathbf{k}, E) \approx \frac{\Gamma_\alpha}{(E - E_\alpha(\mathbf{k}))^2 + (\Gamma_\alpha/2)^2}. \quad (8.29)$$

In Eq. (8.16) it is assumed that the spectral functions are equally populated in energy, or expressed in lesser Green's function,

$$G_{\alpha\alpha}^<(\mathbf{k}, E) = if_{\alpha,\mathbf{k}}A_\alpha(\mathbf{k}, E). \quad (8.30)$$

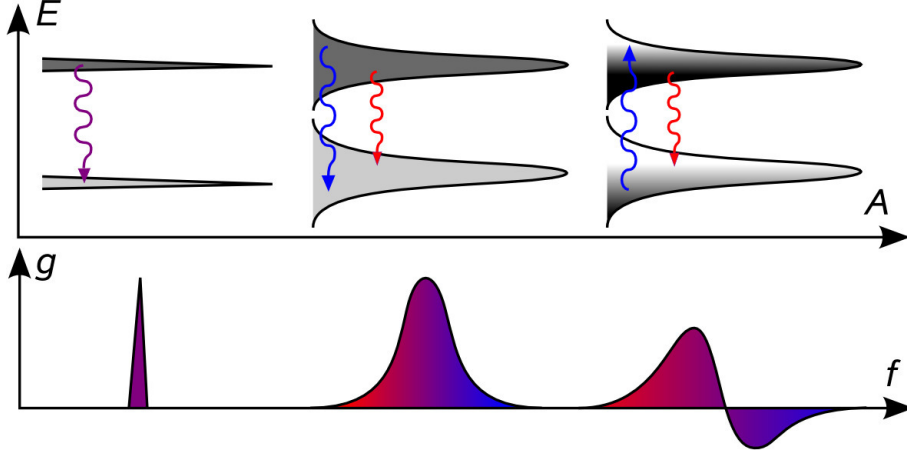


Figure 8.1: Density of states combined with occupation probability in grey-scale (upper panel) and gain spectrum (lower panel) for different levels of description for the gain in a two level system. *Left*: two pure levels. *Center*: Broadened levels. *Right*: Broadened levels with energy-dependent occupations  $f_{\mathbf{k}}(E)$ .

This is an excellent approximation if the scattering strength,  $\Gamma$ , is much less than the temperature,  $k_B T$ . If this is not the case, the above expression must be modified. If the state  $|\alpha, \mathbf{k}\rangle$  is coupled to a reservoir of particles, in this case phonons, the level occupation function,  $f_{\alpha, \mathbf{k}}$ , becomes energy dependent,

$$G_{\alpha\alpha}^<(\mathbf{k}, E) = i f_{\alpha, \mathbf{k}}(E) A_{\alpha}(\mathbf{k}, E), \quad (8.31)$$

which can be interpreted as the low energy part of the state as a higher average occupation than the high energy part.

This effect in lasers gives rise to *dispersive gain* [81]. If the two lasing states have similar populations,  $f_{u, \mathbf{k}} \approx f_{l, \mathbf{k}}$ , both absorption and gain can occur at the same time between the two states, see Fig. 8.1. In most situations,  $f_{\alpha, \mathbf{k}}(E)$  is decreasing with  $E$ , which can give rise to gain at the low energy side of the transition and absorption at the high energy side.

Dispersive gain in QCLs was first experimentally demonstrated in Ref. [82] and then later in Ref. [83]. The spectral width needs to be larger than the temperature to observe dispersive gain. Thus, the first laser [82] was tailored for strong scattering. As most lasers optimized for technological applications operate at high temperature and are designed for a minimum of scattering for the lasing states, dispersive gain is often not observed. In the optimized laser of Ref. [7], no dispersive gain is observed in simulation, see Fig. 2 in Paper II. This effect does, however, result in a red shift of the peak gain of  $\sim 1$  meV and is therefore of importance in quantitative gain calculations.

## 8.5 Spatially Resolved Gain

In order to pinpoint the spatial location of different spectroscopic features without resorting to investigating the absorption/gain between every pair of states, an expression for the spatially resolved gain has been derived. Studying every possible transition in the complex subband system of a mid-IR QCL with approx. 15 subbands per period, see Paper I, is cumbersome due to the many anti-crossings when changing the bias.

The derivation of spatially resolved gain starts with the relation between conductivity and gain, Eq. (8.10), as can be seen in the Appendix of the Paper I. If the current is in phase with the applied oscillating electric field, energy is being accumulated in the material and hence absorption is measured, and vice versa. The conductivity is calculated through the current response of the QCL system due to a small oscillation electric field, and finally, the conductivity can easily be spatially resolved through the spatially resolved current operator.

The expression for spatially resolved gain derived in Paper I is consistent with the standard gain expression, *i.e.*, averaging the spatially resolved gain over the laser structure gives the standard gain expression. However, it is not clear if the spatially resolved gain can be measured, or if it is just a quantity of theoretical interest. For instance, a single transition can exhibit both gain and absorption in different spatial regions.

# 9

## Temperature in THz Lasers

As mentioned in Chap. 3, the mid-IR QCL is now a fairly mature technology with devices that work up to and above room temperature. The THz devices are, however, still bound by low operating temperatures. To this date, the highest reported operation temperature is, without the use of strong magnetic fields, 186 K in pulsed mode [19]. When the laser is pulsed, there is a period of time between the laser pulses to cool down the device, hence higher operating temperature. The quest toward higher temperatures has shown the empirical relation [15],

$$k_B T_{\max} \lesssim \hbar f_{\text{las}}, \quad (9.1)$$

namely, that the maximum lasing temperature is approximately limited by the lasing frequency. To the authors knowledge there are no generally accepted explanations for this trend.

Temperature in QCLs is a complicated quantity, partly because of a strong temperature gradient between the electron system and the heat-sink and partly because the laser, by definition, is in a non-equilibrium state. Often, three temperatures are used in the literature: heat-sink, lattice and electron temperatures.

Under operating conditions, the laser is usually in contact with some thermal reservoir. For instance, at low temperatures the laser might be in contact with liquid helium or liquid nitrogen. In these cases the heat-sink temperature would be 4 and 77 K, respectively. This temperature is usually easy to determine in experiments and is often stated in publications.

The lattice temperature is the temperature of the atomic lattice inside the laser. The occupation of phonon modes are exponentially dependent on this temperature. Since phonon scattering is a strong electron relaxation process, this temperature is important. In phonon depopulation designs, electrons emit optical phonons at a high rate, which can cause a substantial deviation from the equilibrium phonon distribution [84].

Finally, the electron temperature is the temperature of the electrons contributing to lasing and current in the laser device. The electrons are generally far from equilibrium and often subband temperatures are mentioned, referring

to the temperature of each subband. Scattering within each subband is generally much stronger than between subbands, so electrons in different wave vector states within a single subband are usually in quasi-equilibrium [47].

Under operating conditions, there is a strong temperature gradient between the electron system and the heat sink. The exact temperature difference is dependent on many laser and material parameters, such as laser design, materials, operating bias, etc. A rule of thumb is that the electron temperature is approximately 30-50 K higher than the heat-sink temperature [85]. Photoluminescence measurements have shown that the different subband temperatures differ strongly under operation condition in RP THz QCLs, the lasing subbands are 100 K warmer than the lattice, while the injector subband temperature is only slightly elevated [86]. However, the error bars are large in these experiments.

The limited temperature range of operation for THz QCLs together with the complexity of the device have led the way for theoretical studies in order to pinpoint the source of the fast temperature degradation [87–90]. Three causes are usually mentioned: Thermal backfilling, lifetime broadening, and new transport channels at higher temperatures.

## 9.1 Thermal Backfilling

The first experimentally realized QCL was a mid-IR device that lased up to 90 K in pulsed mode [1]. What successfully brought the operating range of the mid-IR device up to room temperature, and beyond, in continuous operation was the double phonon resonance [91]. This means that a second ejector subband was placed two optical phonon energies below the lower laser subband and, hence, a more efficient depopulation of the lower laser subband was achieved.

Neglecting the wave vector dependence, the emission rate of longitudinal optical phonons is proportional to  $1 + n_{LO} \approx 1 + e^{-E_{LO}/k_B T}$  where the first term corresponds to spontaneous emission and the second to stimulated emission. Phonon absorption is proportional to  $n_{LO}$ . At room temperature and an optical phonon energy of 36 meV,  $n_{LO} = 0.25$  and the emission and absorption rates become comparable. Therefore, with a single ejector subband, at room temperature, a substantial amount of electrons from the ejector subband absorb phonons and are re-injected to the lower laser subband. This effect lowers the population inversion and is called *thermal backfilling*, see Fig. 9.1(b).

With the double phonon resonance, electrons in the lowest of the two ejector subbands have to absorb two phonons in order to be re-injected into the lower laser subband, which is a more unlikely process.

Due to the success with the mid-IR device, the double phonon resonance scheme was tried out to increase the maximum operating temperature of the THz devices [92]. This did, however, not improve the temperature performance

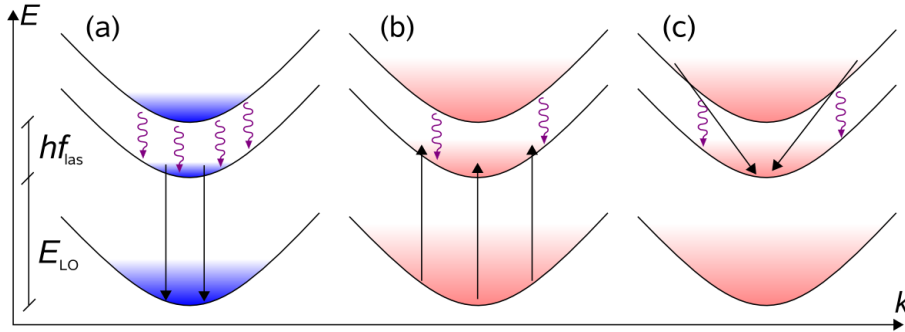


Figure 9.1: Temperature degrading effects. (a) *Intended laser operation* at low temperatures. A low population in the lower laser subband is obtained by tailoring the structure so that an ejector subband is located one optical phonon energy below. Electrons then relax by emitting optical phonons (black arrows). (b) *Thermal backfilling*. At elevated temperatures, electrons in the extractor subband can absorb phonons and get reinjected into the lower laser subband. This effect will decrease the population inversion and, thereby, degrade the lasing properties. (c) *Thermally activated optical phonon emission*. When the temperature increase, the average kinetic energy of the electrons in the upper laser subband increases and electrons with a kinetic energy of more than  $E_{LO} - hf_{las}$  can emit longitudinal optical phonons and relax to the lower laser subband, which would strongly decrease the population inversion.

of the device and suggested that the temperature limiting effect in RP THz QCLs is not thermal backfilling. It is probable that this effect is what limits high temperature operation for other designs with smaller energy difference between the lower laser subband and the upper laser subband of next period.

## 9.2 Thermally Activated Phonon Emission

A second effect, first seen in a simulation by Indjin *et. al.* [87], is that at higher temperatures the average kinetic energy of electrons in the upper laser subband is higher, and these can emit optical phonons and relax down to the bottom of the lower laser subband, see Fig. 9.1(c). This effect has also been quantified by others [88,90] and is well explained in Ref. [93].

The free in-plane motion gives rise to a continuous, and constant, density of states in each subband. This continuum is responsible for the many scattering possibilities that are necessary for the degradation process described above. A way to suppress the scattering is to change the density of states by applying



a strong magnetic field perpendicular to the layers. This field will force the electrons into cyclotron motion and the constant density of states will be split up into discrete Landau Levels (LLs), where the spacing between two neighboring levels is  $\hbar eB/m^*$ . If the energy difference of the LLs is larger than the temperature most electrons will reside in the lowest LL. This discrete density of state will quench thermally activated phonon emission and strong magnetic field has successfully raised the maximum operating temperature to 225 K at 19.3 T [17].

The cyclotron motion will also spatially localize electrons in-plane to the length scale  $l = \sqrt{\hbar/eB} = 25.7/B^{1/2}$  nmT<sup>1/2</sup>. At 30 T, the localization to  $\sim 5$  nm will also lower scattering since the interface roughness length scale is  $l_{i.r.} \approx 10$  nm and the average nearest neighbor distance between two ionized dopants at a sheet doping concentration of  $n = 10^{10}$  cm<sup>-2</sup> is  $l_{dop.} = 1/2\sqrt{n} = 50$  nm [94]. Transport properties of QCLs under strong magnetic field have been studied theoretically in Ref. [95] using a density matrix formalism including phonon scattering.

The major drawback with this method is the extremely high magnetic fields; If the LL spacing must be greater than temperature then,

$$B \gtrsim \frac{m^*k_B}{e\hbar}T \equiv \alpha T, \quad (9.2)$$

where  $\alpha_{\text{GaAs}} \sim 0.05$  T/K. A magnetic field of more than 10 T is thus necessary to reach 200 K. This magnetic field strength strongly limits any future practical application of the device.

This mechanism explains the empirical relation  $hf_{\text{las}} \gtrsim k_B T_{\text{max}}$  quite poorly, because this effect would be weaker for lasers with lower frequencies. The experimental argument in favor of this mechanism is the empirical temperature dependence of the threshold current density,

$$J_{\text{t.h.}} \propto e^{T/T_0}. \quad (9.3)$$

The threshold current density is the current density necessary to reach lasing and  $T_0$  is then a measure of the robustness of the laser with respect to temperature. Low frequency lasers, where thermally activated phonon emission is expected to be small, indeed show high temperature robustness, *i.e.*, large  $T_0$ , even though these lasers have smaller maximum operating temperature, see, *e.g.*, Fig. 5(b)b in Ref. [15]. It is however likely that this effect is what limits THz lasers at higher frequencies.

A second approach is to lower the spatial overlap between the upper and lower laser subband and thereby reduce phonon scattering. This scheme has given the maximum lasing temperature of 186 K [19], without magnetic field. This approach can, however, lower the dipole matrix element and thereby degrade lasing.

A third avenue towards higher temperatures can be to change material system from gallium arsenide (AlGaAs/GaAs) to gallium nitride (AlGaN/GaN) [63, 96, 97]. In standard interband laser technology, GaN is advantageous for its large band gap and hence the high frequency of the emitted light. Here, GaN is interesting for its large optical phonon energy,  $\sim 90$  meV compared to  $\sim 40$  meV in GaAs- and InP-based designs. A higher optical phonon energy would require more kinetic energy of an electron to relax from the upper to the lower laser subband and is therefore expected to yield better temperature performance.

### 9.3 Spectral Broadening and Temperature Dependence of Screening

This mechanism was introduced in Paper II and studied in more detail in Paper V. As the electrons increase their average kinetic energy with increasing temperature, they are less affected by any perturbing scattering potentials. This will decrease screening and enhance scattering. Enhanced scattering will then increase the width of the gain peak and lower the peak value. Regarding the dominant intrasubband scattering effect for THz QCLs in our simulations, impurity scattering, the temperature dependence becomes particularly simple with the Debye approximation, see Chap. 7.

This temperature degrading mechanism differs from all others presented here in that it works independent of population inversion. The main issue here is that calculating the linewidth of THz QCLs is complicated due to correlation effects, see Chap. 8.

### 9.4 Broadening and Resonant Injection

Increased scattering with temperature does not only lead to a broadening of the optical spectra, but also give rise to an uncertainty of the energy of the electrons. Many of the scattering mechanism in these devices are inelastic, meaning that the energy of the electron before and after the scattering event is the same. These scattering mechanisms are impurity, interface roughness and alloy scattering. Also, tunneling between states are strongly enhanced if the two states are aligned. This is often used when designing QCLs, *e.g.*, the injector subband is aligned with the upper laser subband in order to efficiently fill the upper laser subband with electrons and not the lower laser subband.

When the temperature is increased, the energetic width of the states increase and resonant injection exclusively into the upper laser level can be more difficult to achieve. As the energetic width of the two lasing states are comparable with their energy difference, electrons can be injected directly into the

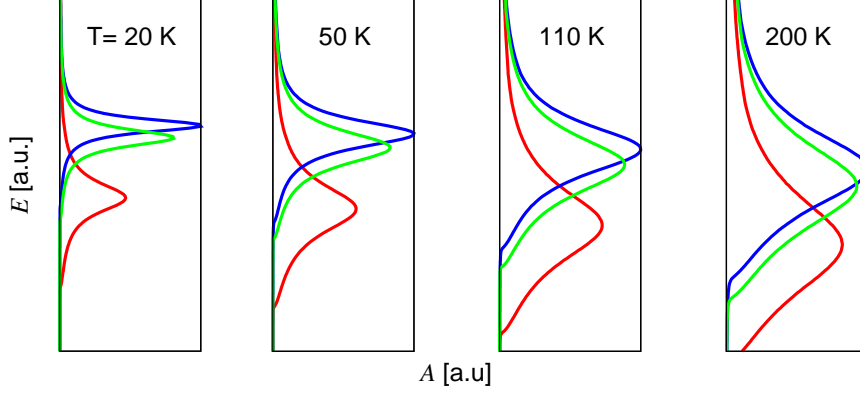


Figure 9.2: Spectral function,  $A_\alpha(\mathbf{k}, E)$  for the injector (green), upper (blue) and lower (red) laser state at  $E_{\mathbf{k}} = 10$  meV for the device presented in Ref [7]. With increasing temperature the width of each state increases and at higher temperature there is a substantial energetic overlap between the injector and lower laser state. This situation would facilitate injection of electrons directly into the lower laser subband, which would be followed by a lowering of the population inversion and lasing performance. The largest width is observed in the lower laser subband since the successful design of the laser has given a fast extraction rate from this subband. Similarly, the smallest width (longest lifetime) is observed in the upper laser subband.

lower laser level, which would lower the population inversion, see Fig. 9.2.

This mechanism would qualitatively explain the empirical relation, Eq. (9.1), that the maximum lasing temperature is approximately limited by the lasing frequency, since the broadening basically scales linearly with temperature,  $\Gamma \propto T$ . Also, the current high temperature record [19], was obtain by making the lasing transition more diagonal by decreasing the spatial overlap between the lasing subbands. As the authors of Ref. [19] point out, this is expected to lower the effect from thermally activated phonon emission. An alternative explanation can be that this also lowers the spatial overlap between the injector and lower lasing subband and hence decrease electron injection directly into the lower laser subband.

# 10

## Summary and Outlook

This thesis deals with transport and optics in Quantum Cascade Lasers (QCLs). This device is a new, unipolar semiconductor laser in which the lasing occurs between subbands formed in quantum wells. Since the first realization in 1994, the high frequency mid-IR QCL now operates above room temperature and is commercially available. In spite of intense research efforts the low frequency THz QCL is still bound by low operating temperatures and currently only operate below 200 K. Experiments suggest that maintaining a population inversion at an energy difference below  $k_B T$  is difficult in these systems, although there is no known reason for this. This open problem, in these rather complicated heterostructures far from equilibrium, calls for theoretical modeling to gain a better understanding of the limiting factors. Most complications, and interesting physics, stem from the fact that the temperature, the level spacing and the scattering are of the same order of magnitude in these systems.

To investigate this problem the physics of QCLs was presented and discussed in this thesis. After a short review of the laser, heterostructures, and relevant scattering mechanisms, the theory of Non-Equilibrium Green's Functions (NEGF) was briefly explained and compared to alternative transport approaches. The main advantage of NEGF is that energetic broadening of the states is included, which is essential for describing transport in THz QCLs, where the broadening is of the order of the typical subband spacing.

Different aspects of optics and temperature dependent processes in QCLs were then discussed later chapters. The focus was put on the temperature dependence of screening and the way this affect the spectral features and transport. In Papers II and V it is found that the impurity scattering strength is strongly enhanced with temperature. The way in which this scattering mechanism is expected to reflect in the optical spectra is difficult to estimate due to correlation effects, see Paper IV. Along the same lines, the impact of acoustic phonon scattering is investigated in Paper III, and is found to play a secondary role.

A next step in this work would be to study the effects of dynamical screening. Also, the effect of broadening on screening would be both interesting and

relevant in THz QCLs. Calculating the dynamically screened electron-electron interaction and impurity scattering within the random phase approximation (RPA) is a trivial extension of the work presented in Paper V. However, how to relate the dynamical scattering matrix elements to any observable, such as linewidths or scattering rates, is not straightforward. As a first approximation, broadening can be included in screening by a finite imaginary part in the denominator of the RPA polarization function.

A longer term goal is to include screening self-consistently in the transport simulations based on NEGF. However, this transport model, without many-body effects, is already numerically demanding and including anisotropic screening calls for efficient approximations that still capture the important features.

# Appendices



# A

## Polarization Function

### The RPA polarization function in the Boltzmann limit

In this work, the most complete model for the polarization function is the RPA approximation,

$$\Pi_{\alpha\beta}(\mathbf{q}, E) = \lim_{\gamma \rightarrow 0^+} \frac{2}{A} \sum_{\mathbf{k}} \frac{f_{\alpha, \mathbf{k}+\mathbf{q}} - f_{\beta, \mathbf{k}}}{E_{\alpha, \mathbf{k}+\mathbf{q}} - E_{\beta, \mathbf{k}} - E - i\gamma}. \quad (\text{A.1})$$

In this section, an efficient way of evaluating this expression in the Boltzmann limit will be explained.

The Boltzmann limit is an excellent approximation in THz QCLs because the strong intraband electron-electron scattering thermalizes each subband [51], and, also, the average occupation is low at the elevated temperatures of interests, *i.e.*,

$$f_{\alpha, \mathbf{k}} \approx \frac{1}{e^{\beta_{\alpha}(E_{\mathbf{k}} - \mu_{\alpha})} + 1} \approx e^{-\beta_{\alpha}(E_{\mathbf{k}} - \mu_{\alpha})}, \quad (\text{A.2})$$

where  $\mu_{\alpha}$  is the chemical potential of subband  $\alpha$  and  $\beta_{\alpha} = 1/k_B T_{\alpha}$ . In the Boltzmann limit, the polarization function becomes particular simple to evaluate. This method was first described by Lee and Galbraith in Sect. 2B of Ref. [98], where only two subbands are studied, with the same temperature and chemical potential. Here, the expression will be generalized to systems where each subband has arbitrary temperature and chemical potential, relevant for describing screening in THz QCLs.

Since both the occupation and subband energy are only functions of the magnitude of momentum, the quantity

$$\tilde{\Pi}_{\alpha\beta}^{\pm}(\mathbf{q}, E) = \lim_{\gamma \rightarrow 0^+} \frac{2}{A} \sum_{\mathbf{k}} \frac{f_{\alpha, \mathbf{k}}}{E_{\alpha, \mathbf{k}} - E_{\beta, \mathbf{k}+\mathbf{q}} \pm E \pm i\gamma}, \quad (\text{A.3})$$



can be investigated since  $\Pi_{\alpha\beta}(\mathbf{q}, E) = \tilde{\Pi}_{\alpha\beta}^-(\mathbf{q}, E) + \tilde{\Pi}_{\beta\alpha}^+(\mathbf{q}, E)$ . One crucial approximation is that all subbands have the same in-plane effective mass,  $m^*$ . If this approximation is relaxed, the denominator in  $\tilde{\Pi}_{\alpha\beta}^\pm$  will be a second order polynomial in  $\mathbf{k}$ , instead of a first order, which will make efficient evaluation more complicated.

With equal effective mass,

$$\tilde{\Pi}_{\alpha\beta}^\pm(\mathbf{q}, E) = \lim_{\gamma \rightarrow 0^+} \frac{2}{A} \sum_{\mathbf{k}} \frac{f_{\alpha, \mathbf{k}}}{\Delta E_{\alpha\beta} - E_{\mathbf{q}} - \hbar^2 \mathbf{k} \cdot \mathbf{q} / m^* \pm E \pm i\gamma}, \quad (\text{A.4})$$

where  $\Delta E_{\alpha\beta} = E_\alpha - E_\beta$ . In the continuum limit, with radial coordinates,

$$\sum_{\mathbf{k}} = \frac{A}{(2\pi)^2} \int d^2\mathbf{k} = \frac{A}{(2\pi)^2} \int_0^\infty dk \int_0^{2\pi} d\theta k, \quad (\text{A.5})$$

Eq. (A.4) becomes

$$\tilde{\Pi}_{\alpha\beta}^\pm(q, E) = \lim_{\gamma \rightarrow 0^+} \frac{2}{(2\pi)^2} \int_0^\infty dk \int_0^{2\pi} d\theta \frac{k f_{\alpha, k}}{\Delta E_{\alpha\beta} - E_q - \hbar^2 k q \cos \theta / m^* \pm E \pm i\gamma}. \quad (\text{A.6})$$

This, together with the relation

$$\lim_{\gamma \rightarrow 0^+} \frac{1}{E - E_0 \pm i\delta} = \mathcal{P} \frac{1}{E - E_0} \pm i\pi \delta(E - E_0), \quad (\text{A.7})$$

the real and imaginary part are

$$\begin{aligned} \Re \left\{ \tilde{\Pi}_{\alpha\beta}^\pm(q, \omega) \right\} &= \frac{2}{(2\pi)^2} \int_0^\infty dk \mathcal{P} \int_0^{2\pi} d\theta \frac{k f_{\alpha, k}}{\Delta E_{\alpha\beta} - E_q - \hbar^2 k q \cos \theta / m^* \pm E}, \\ \Im \left\{ \tilde{\Pi}_{\alpha\beta}^\pm(q, \omega) \right\} &= \pm \frac{1}{2\pi} \int_0^\infty dk \int_0^{2\pi} d\theta k f_{\alpha, k} \delta(\Delta E_{\alpha\beta} - E_q - \hbar^2 k q \cos \theta / m^* \pm E). \end{aligned} \quad (\text{A.8})$$

## Useful Integrals

In this derivation a few mathematical identities will be used. First,

$$\mathcal{P} \int_0^{2\pi} \frac{dx}{a + b \cos x} = \begin{cases} 0 & \text{if } a^2 < b^2 \\ \text{sign}\{a\} \frac{2\pi}{\sqrt{a^2 - b^2}} & \text{if } a^2 > b^2 \end{cases}, \quad (\text{A.9})$$

secondly,

$$\int_0^{2\pi} d\theta \delta(a \cos \theta - b) = \begin{cases} 0 & \text{if } a^2 < b^2 \\ \frac{2}{\sqrt{a^2 - b^2}} & \text{if } a^2 > b^2 \end{cases}, \quad (\text{A.10})$$

and third, the integral

$$\int_1^\infty dx \frac{e^{-\mu x}}{\sqrt{x-1}} = \sqrt{\frac{\pi}{\mu}} e^{-\mu}, \quad \text{if } \Re\{\mu\} > 0, \quad (\text{A.11})$$

will be used. Last, the *confluent hypergeometric function of first kind*,  $\Phi(\alpha, \beta; z)$ <sup>1</sup>, is introduced, with the integral representation, see, *e.g.*, Eq. (13.2.1) in Ref. [99],

$$\Phi(\alpha, \beta; z) = \frac{\Gamma(\beta)}{\Gamma(\beta-\alpha)\Gamma(\alpha)} \int_0^1 e^{zt} t^{\alpha-1} (1-t)^{\beta-\alpha-1} dt. \quad (\text{A.12})$$

For  $\alpha = 1$ ,  $\beta = 3/2$  and with the variable substitution  $v = zt$ , the function becomes,

$$\Phi\left(1, \frac{3}{2}; z\right) = \frac{1}{2} \frac{1}{\sqrt{z}} \int_0^z \frac{e^v}{\sqrt{z-v}} dv, \quad (\text{A.13})$$

and with a negative argument,

$$\Phi\left(1, \frac{3}{2}; -z\right) = \frac{1}{2} \frac{1}{\sqrt{z}} \int_0^z \frac{e^{-v}}{\sqrt{z-v}} dv. \quad (\text{A.14})$$

The advantage with expressing the complicated integrals in the expression for the polarization function as confluent geometric functions is that there are numerical software packages, well tested and optimized, for evaluating these functions, see, *e.g.*, Ref. [100]. These functions are often evaluated via a Taylor expansion,

$$\Phi(\alpha, \beta; z) = 1 + \frac{\alpha}{\beta} \frac{z}{1!} + \frac{\alpha(\alpha+1)}{\beta(\beta+1)} \frac{z^2}{2!} + \frac{\alpha(\alpha+1)(\alpha+2)}{\beta(\beta+1)(\beta+2)} \frac{z^3}{3!} + \dots \quad (\text{A.15})$$

With the expansion above, all terms in the series have the same sign for positive  $z$ , so rapid convergence is expected. For negative  $z$ , the terms in the series have alternating signs, which can result in cumbersome numerics. Here, the relation, Eq. (13.2.27) in Ref. [99],

$$\Phi(\alpha, \beta; z) = e^z \Phi(\beta - \alpha, \beta; -z), \quad (\text{A.16})$$

can be used for faster convergence.

---

<sup>1</sup>Alternative name and notations are Kummer's function,  ${}_1F_1(\alpha, \beta; z)$  and  $M(\alpha, \beta; z)$

### Final expression

With the use of the integrals above the polarization function, in the Boltzmann limit, becomes

$$\begin{aligned} \Pi_{\alpha\beta}(q, E) = & -\frac{1}{8\pi} \frac{2m^*}{\hbar^2} \\ & \times \left( e^{\beta\alpha\mu_\alpha} \left[ \frac{E_+}{E_q} \Phi \left( 1; \frac{3}{2}; -\frac{\beta_\alpha E_+^2}{4 E_q} \right) + i \sqrt{\frac{\pi}{\beta_\alpha E_q}} \exp \left[ -\frac{\beta_\alpha E_+^2}{4 E_q} \right] \right] \right. \\ & \left. + e^{\beta\beta\mu_\beta} \left[ \frac{E_-}{E_q} \Phi \left( 1; \frac{3}{2}; -\frac{\beta_\beta E_-^2}{4 E_q} \right) - i \sqrt{\frac{\pi}{\beta_\beta E_q}} \exp \left[ -\frac{\beta_\beta E_-^2}{4 E_q} \right] \right] \right), \end{aligned} \quad (\text{A.17})$$

where,  $E_\pm = E_q \pm \Delta E_{\beta\alpha} \pm E$ . The Boltzmann limit can be relaxed for evaluation of the polarization function for general occupations. Still, the angular integrals, Eqs. (A.9) and (A.10), can be evaluated analytically while the integration over  $k$  have to be calculated numerically. This has been performed for Fermi-Dirac distributions for the devices in Paper V, however, with negligible corrections.

### The static RPA polarization function in the long wavelength limit

A popular approximation for transport in QCLs is the long wavelength limit [71,98],

$$\begin{aligned} \Pi_{\alpha\beta}(\mathbf{q} \rightarrow 0, E = 0) &= \frac{2}{A} \sum_{\mathbf{k}} \frac{f_{\alpha,\mathbf{k}} + \mathbf{q} \cdot \nabla_{\mathbf{k}} f_{\alpha,\mathbf{k}} - f_{\beta,\mathbf{k}}}{E_{\alpha,\mathbf{k}} + \mathbf{q} \cdot \nabla_{\mathbf{k}} E_{\alpha,\mathbf{k}} - E_{\beta,\mathbf{k}}} \\ &= \begin{cases} -\frac{m^*}{\pi \hbar^2} f_{\alpha,\mathbf{k}=0} & \text{if } \alpha = \beta \\ \frac{n_\alpha - n_\beta}{\Delta E_{\alpha,\beta}} & \text{if } \alpha \neq \beta, \end{cases} \end{aligned} \quad (\text{A.18})$$

where  $n_\alpha$  is the subband concentration,

$$n_\alpha = \frac{2}{A} \sum_{\mathbf{k}} f_{\alpha,\mathbf{k}}. \quad (\text{A.19})$$

For the diagonal polarization functions  $\nabla_{\mathbf{k}} f_{\alpha,\mathbf{k}} = (\nabla_{\mathbf{k}} E_{\alpha,\mathbf{k}}) \partial f_{\alpha,\mathbf{k}} / \partial E_{\alpha,\mathbf{k}}$  has been used together with

$$\frac{2}{A} \sum_{\mathbf{k}} \frac{\partial f_{\alpha,\mathbf{k}}}{\partial E_{\alpha,\mathbf{k}}} = \frac{2}{A} \sum_{\mathbf{k}} \frac{\partial f_{\alpha,k}}{\partial k} \frac{\partial k}{\partial E} = \frac{1}{\pi} \int_0^\infty dk k \frac{\partial f_{\alpha,k}}{\partial k} \frac{m^*}{\hbar^2 k} = -\frac{m^*}{\pi \hbar^2} f_{\alpha,k=0}. \quad (\text{A.20})$$

This long wavelength limit is an excellent approximation regarding static screening, see Paper V.

# B

## Coulomb Interaction Matrix Elements

In screening and electron-electron scattering the necessary matrix elements that need to be evaluated are

$$V_{ijkl}(q) = \frac{e^2}{2A\varepsilon_0\varepsilon_r} \frac{F_{ijkl}(q)}{q}, \quad (\text{B.1})$$

where all constants have their usual meaning and the form factors,  $F$ , are

$$F_{ijkl}(q) = \int dz_1 \int dz_2 \psi_i^*(z_1) \psi_j(z_1) e^{-q|z_1-z_2|} \psi_k^*(z_2) \psi_l(z_2). \quad (\text{B.2})$$

Brute force computation can be quite lengthy due to the double integral and the four indices. With  $N_z = 3000$   $z$ -points, a total of  $10^6$  terms are added for each form factor, which can be time-consuming, since with  $N_q = 1000$   $q$ -points and  $N_\nu = 20$  states, there are  $1.6 \cdot 10^8$  of them. A method presented by Bonno, Thobel and Dessenne [47] strongly ease the numerical burden with these form factors. This method is based on the fact that the wave functions are usually smooth in the  $z$ -direction and can, therefore, be approximated well by only the lowest Fourier components. Also, the factor in Fourier space corresponding to  $e^{-q|z_1-z_2|}$  in real space in Eq. (B.2) can be factorized, such that the double sum becomes only five single sums. In this appendix the method will be explained in more detail.

A fast Fourier transform of every wave function pair gives

$$\psi_i^*(z) \psi_j(z) = \sum_{\sigma=-N_H}^{N_H} \gamma_{\sigma}^{ij} e^{ik_0\sigma z}, \quad (\text{B.3})$$

where  $k_0L = 2\pi$  and  $L$  is the size of the wave functions in  $z$ -direction. The wave functions are usually very well-behaved functions of  $z$  and only a few of the lowest Fourier components are needed to quantitatively approximate the

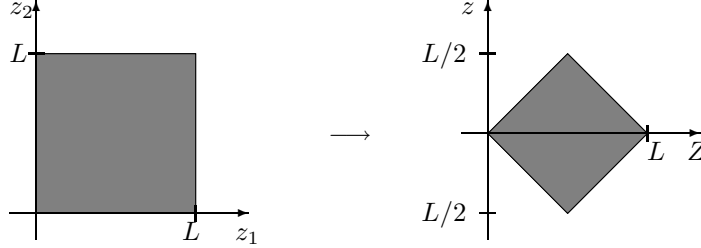
wave functions, *i.e.*,  $N_H \ll N_z/2$ . Eq. (B.2) then becomes

$$\begin{aligned} F_{ijkl}(q) &= \sum_{\sigma_1} \sum_{\sigma_2} \gamma_{\sigma_1}^{ij} \gamma_{\sigma_2}^{kl} \int_0^L dz_1 \int_0^L dz_2 e^{ik_0 z_1 \sigma_1} e^{-q|z_1 - z_2|} e^{ik_0 z_2 \sigma_2} \\ &\equiv \sum_{\sigma_1} \sum_{\sigma_2} \gamma_{\sigma_1}^{ij} \gamma_{\sigma_2}^{kl} G_{\sigma_1 \sigma_2}(q), \end{aligned} \quad (\text{B.4})$$

where a closed expression for  $G_{\sigma_1 \sigma_2}(q)$  will be derived.

A first step is the variable change

$$\begin{cases} Z = (z_1 + z_2)/2 \\ z = (z_1 - z_2)/2 \end{cases} \quad \begin{cases} z_1 = Z + z \\ z_2 = Z - z \end{cases} \quad (\text{B.5})$$



This variable change gives a factor of 2 in the integral and the result is

$$G_{\sigma_1 \sigma_2}(q) = 2 \int_0^L dZ e^{ik_0(\sigma_1 + \sigma_2)Z} \int_{-\min\{Z, L-Z\}}^{\min\{Z, L-Z\}} dz e^{-q|z|} e^{ik_0(\sigma_1 - \sigma_2)z}. \quad (\text{B.6})$$

Evaluating these two integrals is now straightforward and the result is

$$G_{\sigma_1 \sigma_2}(q) = \frac{2Lq\delta_{\sigma_1, -\sigma_2}}{q^2 + \sigma_2^2 k_0^2} + \frac{2(e^{-qL} - 1)(q^2 + \sigma_1 \sigma_2 k_0^2)}{(q^2 + \sigma_1^2 k_0^2)(q^2 + \sigma_2^2 k_0^2)}. \quad (\text{B.7})$$

The main advantage here is that the double sum, Eq. (B.4), over the first term in  $G_{\sigma_1 \sigma_2}(q)$  becomes a single sum due to the Kronecker delta function. The second term can be split in two and then factorized in parts only functions of either  $\sigma_1$  or  $\sigma_2$ ,

$$2q^2(e^{-qL} - 1) \frac{1}{q^2 + \sigma_1^2 k_0^2} \cdot \frac{1}{q^2 + \sigma_2^2 k_0^2} + 2(e^{-qL} - 1) \frac{\sigma_1 k_0}{q^2 + \sigma_1^2 k_0^2} \cdot \frac{\sigma_2 k_0}{q^2 + \sigma_2^2 k_0^2}. \quad (\text{B.8})$$

Thus, the double sum in Eq. (B.4) becomes only five single sums. The result is a sum with  $10^3$  terms for  $N_H = 100$ , instead of  $10^7$  as a brute force integration would require. The factor  $10^4$  increase in computational speed is quite substantial and can turn a week of computation into a minute.

---

There are a few symmetries that can simplify calculations even further, *e.g.*,  $\gamma_{\sigma}^{ij} = (\gamma_{-\sigma}^{ji})^*$  and for real wave functions  $\gamma_{\sigma}^{ij} = \gamma_{\sigma}^{ji}$ . Also, if  $N_{\text{per}}$  states per period are included,  $\gamma_{\sigma}^{i+N_{\text{per}}:j+N_{\text{per}}} = e^{ik_0 d} \gamma_{\sigma}^{i,j}$  where  $d$  is the length of one period. In this context, one should, however, not forget the implicit periodic boundary conditions in the  $z$ -direction imposed by the discrete Fourier transform, Eq. (B.3).

An alternative approach to efficiently calculate the Coulomb matrix elements has been proposed by Pereira *et. al.* [101]. The idea is that the main matrix elements are calculated in the two limits,  $q \rightarrow 0$  and  $q \rightarrow \infty$ , and then interpolated for finite  $q$ .

## References

- [1] J. Faist, F. Capasso, D. L. Sivco, C. Sirtori, A. L. Hutchinson, and A. Y. Cho, *Science* **264**, 553 (1994).
- [2] L. Esaki and R. Tsu, *IBM J. Res. Develop.* **14**, 61 (1970).
- [3] R. F. Kazarinov and R. A. Suris, *Sov. Phys. Semicond.* **5**, 707 (1971).
- [4] R. F. Kazarinov and R. A. Suris, *Sov. Phys. Semicond.* **6**, 120 (1972), [*Fiz. Tekh. Poluprov.* **6**, 148 (1972)].
- [5] M. Tonouchi, *Nature Photonics* **1**, 97 (2007).
- [6] B. S. Williams, S. Kumar, Q. Hu, and J. L. Reno, *Optics Express* **13**, 3331 (2005).
- [7] S. Kumar, B. S. Williams, Q. Hu, and J. L. Reno, *Appl. Phys. Lett.* **88**, 121123 (2006).
- [8] C. Sirtori, P. Kruck, S. Barbieri, P. Collot, J. Nagle, M. Beck, J. Faist, and U. Oesterle, *Appl. Phys. Lett.* **73**, 3486 (1998).
- [9] I. Vurgaftman, J. R. Meyer, and L. R. Ram-Mohan, *J. Appl. Phys.* **89**, 5815 (2001).
- [10] T. W. Hickmott, P. M. Solomon, R. Fischer, and H. Morkoç, *J. Appl. Phys.* **57**, 2844 (1985).
- [11] O. Cathabard, R. Teissies, J. Devenson, and A. N. Baranov, *The 10th International Conference on Intersubband Transitions in Quantum Wells (ITQW 2009)* (National Research Council, Montreal, Canada, 2009), p. 62.
- [12] C. Walther, M. Fischer, G. Scalari, R. Terazzi, N. Hoyler, and J. Faist, *Appl. Phys. Lett.* **91**, 131122 (2007).
- [13] N. Ulbrich, G. Scarpa, A. Sigl, J. Roskopf, G. Bohm, G. Abstrieter, and M. C. Amann, *Electronics Letters* **37**, 1341 (2001).
- [14] J. Devenson, O. Cathabard, R. Teissier, and A. N. Baranov, *Appl. Phys. Lett.* **91**, 251102 (2007).
- [15] B. S. Williams, *Nature Photonics* **1**, 517 (2007).
- [16] M. A. Belkin, Q. J. Wang, C. Pflugl, A. Belyanin, S. P. Khanna, A. G. Davies, E. H. Linfield, and F. Capasso, *IEEE Journal of Selected Topics in Quantum Electronics* **15**, 952 (2009).

- 
- [17] A. Wade, G. Fedorov, D. Smirnov, S. Kumar, B. S. Williams, Q. Hu, and J. L. Reno, *Nature Photonics* **3**, 41 (2009).
- [18] M. A. Belkin, J. A. Fan, S. Hormoz, F. Capasso, S. P. Khanna, M. Lachab, A. G. Davies, and E. H. Linfield, *Optics Express* **16**, 3242 (2008).
- [19] S. Kumar, Q. Hu, and J. L. Reno, *Appl. Phys. Lett.* **94**, 131105 (2009).
- [20] S. Kumar, C. W. I. Chan, Q. Hu, and J. L. Reno, *Appl. Phys. Lett.* **95**, 141110 (2009).
- [21] J. Faist, *Appl. Phys. Lett.* **90**, 253512 (2007).
- [22] J. R. Freeman, O. Marshall, H. E. Beere, and D. A. Ritchie, *Appl. Phys. Lett.* **93**, 191119 (2008).
- [23] B. Williams, S. Kumar, Q. Hu, and J. Reno, *Electronics Letters* **42**, 89 (2006).
- [24] F. Bloch, *Zeitschrift für Physik A Hadrons and Nuclei* **52**, 555 (1929).
- [25] G. Bastard, *Wave Mechanics Applied to Semiconductor Heterostructures* (Les Editions de Physique, Les Ulis Cedex, France, 1988).
- [26] G. Nenciu, *Rev. Mod. Phys.* **63**, 91 (1991).
- [27] M.-E. Pistol, *Phys. Rev. B* **60**, 14269 (1999).
- [28] P. Harrison, *Quantum Wells, Wires and Dots*, 2nd ed. (John Wiley & Sons, Chichester, England, 2005).
- [29] S. R. White and L. J. Sham, *Phys. Rev. Lett.* **47**, 879 (1981).
- [30] A. Wacker, *Phys. Rep.* **357**, 1 (2002).
- [31] H. Haug and A.-P. Jauho, in *Quantum Kinetics in Transport and Optics of Semiconductors*, Vol. 123 of *Springer Series on Solid-State Sciences*, edited by K. von Klitzing (Springer, Berlin, 1996).
- [32] N. Marzari and D. Vanderbilt, *Phys. Rev. B* **56**, 12847 (1997).
- [33] J. Zak, *Phys. Rev. Lett.* **20**, 1477 (1968).
- [34] T. Kubis, C. Yeh, P. Vogl, A. Benz, G. Fasching, and C. Deutsch, *Phys. Rev. B* **79**, 195323 (2009).
- [35] J. S. Blakemore, *J. Appl. Phys.* **53**, R123 (1982).
- [36] H. Fröhlich, *Advances In Physics* **3**, 325 (1954).



- 
- [37] K. W. Kim and M. A. Stroscio, *J. Appl. Phys.* **68**, 6289 (1990).
- [38] S. Yu, K. W. Kim, M. A. Stroscio, G. J. Iafrate, J.-P. Sun, and G. I. Haddad, *J. Appl. Phys.* **82**, 3363 (1997).
- [39] C. Becker, C. Sirtori, H. Page, A. Robertson, V. Ortiz, and X. Marcadet, *Phys. Rev. B* **65**, 085305 (2002).
- [40] H. Callebaut, S. Kumar, B. S. Williams, Q. Hu, and J. L. Reno, *Appl. Phys. Lett.* **84**, 645 (2004).
- [41] S. Tsujino, A. Borak, E. Müller, M. Scheinert, C. V. Falub, H. Sigg, D. Grützmacher, M. Giovannini, and J. Faist, *Appl. Phys. Lett.* **86**, 062113 (2005).
- [42] A. Wittmann, Y. Bonetti, J. Faist, E. Gini, and M. Giovannini, *Appl. Phys. Lett.* **93**, 141103 (2008).
- [43] D. K. Ferry, S. M. Goodnick, and J. Bird, *Transport in Nanostructures*, 2nd ed. (Cambridge University Press, Cambridge, 2009).
- [44] T. Ando, *J. Phys. Soc. Jpn.* **51**, 3900 (1982).
- [45] N. Regnault, R. Ferreira, and G. Bastard, *Phys. Rev. B* **76**, 165121 (2007).
- [46] H. W. Verleur and A. S. Barker, *Phys. Rev.* **149**, 715 (1966).
- [47] O. Bonno, J.-L. Thobel, and F. Dessenne, *J. Appl. Phys.* **97**, 43702 (2005).
- [48] P. Hyldgaard and J. W. Wilkins, *Phys. Rev. B* **53**, 6889 (1996).
- [49] L. Hedin, *Phys. Rev.* **139**, A796 (1965).
- [50] T. Schmielau and M. F. J. Pereira (unpublished).
- [51] P. Harrison, *Appl. Phys. Lett.* **75**, 2800 (1999).
- [52] C. Jacoboni and L. Reggiani, *Rev. Mod. Phys.* **55**, 645 (1983).
- [53] C. Jacoboni, R. Brunetti, and P. Bordone, in *Theory of Transport Properties of Semiconductor Nanostructures*, Vol. 4 of *Electronic Materials*, edited by E. Schöll (Chapman and Hall, London, 1998), pp. 59–102.
- [54] R. C. Iotti, E. Ciancio, and F. Rossi, *Phys. Rev. B* **72**, 125347 (2005).
- [55] T. Kuhn, in *Theory of Transport Properties of Semiconductor Nanostructures*, Vol. 4 of *Electronic Materials*, edited by E. Schöll (Chapman and Hall, London, 1998), pp. 173–214.

- 
- [56] C. Weber, A. Wacker, and A. Knorr, Phys. Rev. B **79**, 165322 (2009).
- [57] R. Terazzi, T. Gresch, A. Wittmann, and J. Faist, Phys. Rev. B **78**, 155328 (2008).
- [58] L. P. Keldysh, Sov. Phys. JETP **20**, 2578 (1965).
- [59] L. P. Kadanoff and G. Baym, in *Quantum Statistical Mechanics, Frontiers in Physics Series*, edited by D. Pines (W. A. Benjamin, New York, 1962).
- [60] S.-C. Lee and A. Wacker, Phys. Rev. B **66**, 245314 (2002).
- [61] S.-C. Lee, F. Banit, M. Woerner, and A. Wacker, Phys. Rev. B **73**, 245320 (2006).
- [62] T. Schmielau and M. F. Pereira, phys. stat. sol. (b) **246**, 329 (2009).
- [63] C. Gui-Chu and F. Guang-Han, Chinese Physics Letters **25**, 1815 (2008).
- [64] W. Kohn and J. M. Luttinger, Phys. Rev. **108**, 590 (1957).
- [65] A. A. Abrikosov, L. P. Gorkov, and I. E. Dzyaloshinski, *Methods of Quantum Field Theory in Statistical Physics* (Dover, New York, 1975).
- [66] Y. Chen, N. Regnault, R. Ferreira, B.-F. Zhu, and G. Bastard, Phys. Rev. B **79**, 235314 (2009).
- [67] J. B. Khurgin, Appl. Phys. Lett. **93**, 091104 (2008).
- [68] D. Bohm and D. Pines, Phys. Rev. **92**, 609 (1953).
- [69] F. Banit, S.-C. Lee, A. Knorr, and A. Wacker, Appl. Phys. Lett. **86**, 41108 (2005).
- [70] N. D. Mermin, Phys. Rev. B **1**, 2362 (1970).
- [71] J. T. Lü and J. C. Cao, Appl. Phys. Lett. **89**, 211115 (2006).
- [72] J. D. Jackson, *Classical Electrodynamics*, 3rd ed. (John Wiley & Sons, New York, 1998).
- [73] P. A. M. Dirac, Proceedings of The Royal Society of London Series A - Containing Papers of a Mathematical and Physical Character **114**, 243 (1927).
- [74] A. Wacker, Phys. Rev. B **66**, 85326 (2002).
- [75] Z. Fried, Phys. Rev. A **8**, 2835 (1973).

- 
- [76] R. R. Schlicher, W. Becker, J. Bergou, and M. O. Scully, in *Proceedings of the NATO ASI on Quantum Electrodynamics and Quantum Optics, Boulder, Colorado, 1983*, edited by A. O. Barut (Plenum, New York, 1984), pp. 405–441.
- [77] K. Reimann and M. Woerner (unpublished).
- [78] I. Waldmüller, J. Förstner, S.-C. Lee, A. Knorr, M. Woerner, K. Reimann, R. A. Kaindl, T. Elsaesser, R. Hey, and K. H. Ploog, *Phys. Rev. B* **69**, 205307 (2004).
- [79] T. Ando, *J. Phys. Soc. Jpn.* **54**, 2671 (1985).
- [80] O. Svelto, *Principles of Lasers*, 4th ed. (Plenum Press, New York, 1998).
- [81] A. Wacker, *Nature Physics* **3**, 298 (2007).
- [82] R. Terazzi, T. Gresch, M. Giovannini, N. Hoyler, N. Sekine, and J. Faist, *Nature Physics* **3**, 329 (2007).
- [83] D. G. Revin, J. W. Cockburn, M. J. Steer, R. J. Airey, M. Hopkinson, A. B. Krysa, L. R. Wilson, and S. Menzel, *Appl. Phys. Lett.* **90**, 21108 (2007).
- [84] J. T. Lu and J. C. Cao, *Appl. Phys. Lett.* **88**, 061119 (2006).
- [85] C. A. Evans, V. D. Jovanović, D. Indjin, Z. Ikonić, and P. Harrison, *IEEE Journal of Quantum Electronics* **42**, 859 (2006).
- [86] M. S. Vitiello, G. Scamarcio, V. Spagnolo, B. S. Williams, S. Kumar, Q. Hu, and J. L. Reno, *Appl. Phys. Lett.* **86**, 111115 (2005).
- [87] D. Indjin, P. Harrison, R. W. Kelsall, and Z. Ikonić, *Appl. Phys. Lett.* **82**, 1347 (2003).
- [88] J. C. Cao, J. T. Lu, and H. Li, *Physica E* **41**, 282 (2008).
- [89] H. Li, J. C. Cao, Z. Y. Tan, Y. J. Han, X. G. Guo, S. L. Feng, H. Luo, S. R. Laframboise, and H. C. Liu, *J. Phys. D* **42**, 025101 (2009).
- [90] C. Jirauschek and P. Lugli, *phys. stat. sol. (c)* **5**, 221 (2008).
- [91] M. Beck, D. Hofstetter, T. Aellen, J. Faist, U. Oesterle, M. Illegems, E. Gini, and H. Melchior, *Science* **295**, 301 (2002).
- [92] B. S. Williams, S. Kumar, Q. Qin, Q. Hu, and J. L. Reno, *Appl. Phys. Lett.* **88**, 261101 (2006).
- [93] C. Sirtori, *Nature Photonics* **3**, 13 (2009).

- 
- [94] P. Hertz, *Mathematische Annalen* **67**, 387 (1909).
- [95] I. Savić, N. Vukmirović, Z. Ikonić, D. Indjin, R. W. Kelsall, P. Harrison, and V. Milanović, *Phys. Rev. B* **76**, 165310 (2007).
- [96] G. Sun and R. A. Soref, *Microelectronics Journal* **36**, 450 (2005).
- [97] E. Bellotti, K. Driscoll, T. D. Moustakas, and R. Paiella, *Appl. Phys. Lett.* **92**, 101112 (2008).
- [98] S.-C. Lee and I. Galbraith, *Phys. Rev. B* **59**, 15796 (1999).
- [99] M. Abramowitz and I. A. Stegun, *Handbook of Mathematical Functions with Formulas, Graphs, and Mathematical Tables*, 9th ed. (Dover, New York, 1964).
- [100] M. Galassi, J. Davies, J. Theiler, B. Gough, G. Jungman, P. Alken, M. Booth, and F. Rossi, in *GNU Scientific Library Reference Manual*, 3rd ed., edited by B. Gough (Network Theory Ltd., United Kingdom, 2009), p. 592.
- [101] M. F. Pereira, Jr., S.-C. Lee, and A. Wacker, *Phys. Rev. B* **69**, 205310 (2004).
- [102] D. G. Revin, L. R. Wilson, J. W. Cockburn, A. B. Krysa, J. S. Roberts, and R. J. Airey, *Appl. Phys. Lett.* **88**, 131105 (2006).



# Acknowledgments

First, I would like to thank my supervisor Andreas Wacker for introducing me to the field of transport and optics in nanostructures and for always having his door open for questions and discussions. His knowledge, from experimental details to many-body physics and beyond, has been both helpful and inspiring. I would like to thank my co-supervisor, Carl-Olof Almbladh, for discussions on physics, computing, and collaborations in teaching, which I have enjoyed a lot.

The collaboration with Mauro Pereira Jr. at Sheffield Hallam University, and his frequent visits to Lund, have been much appreciated. I am also in debt to him for showing me many nice restaurants in Rio.

There are a few people on the path to this thesis I have had the pleasure of working with that I also would like to thank; Klas Nilsson for being an inspiring physics teacher, Per Granberg for introducing me to solid-state physics, and Mats-Erik Pistol for leading me towards theoretical semiconductor physics.

I have benefitted a lot from being a member of a stimulation and enthusiastic research group. A warm thank you goes to Greta Lindwall, Olov Karlström, Benny Lassen, the new “partner group”; Peter Samuelsson, Franseca Battista, and Christian Bergenfeldt and all colleagues at the Division of Mathematical Physics. A special thank you goes to Carsten Weber for the many discussions about quantum cascade lasers and semiconductor optics that has taught me a lot.

A warm thank you goes to Jonas Pedersen, whom I have had the pleasure to share office with during most of my PhD studies. His refusal to learn Swedish during his four years stay has taught me Danish very well. I have really enjoyed all the shared lunches and the skiing winter school.

I would like to thank my parents, my brother and sister, and friends, for all their love, support and help in many practical matters. Finally, and most importantly, Sara for all her love, for taking care of the home during the writing of this thesis and showing me how to write and defend a thesis on electron transport for laser action. And of course, Hedda for being a wonderful distraction from research.

Lund, November 2009  
Rikard Nelander



**Part B**

**The Papers**





# The Papers — Summary

## Paper I

In 2006, the first spectroscopy experiments on a QCL under operating conditions were presented by D. G. Revin *et. al.* [102]. This provided a new way of characterizing the state of a QCL. Parameters such as gain coefficient, waveguide loss and temperature of the laser can be measured by this method. In order to explain the rather complicated experimental spectra, the spectra is calculated for the same device and its features are thoroughly discussed in this paper. Results at an early stage of this project can be found in Papers VI and VII, not included here.

The key finding is that the evolution of most spectral features with changing bias can be explained by a spatial shift of the electrons from the active region at low bias towards the injector region at higher bias.

I performed the calculations, analyzed the data, and wrote a large part of the paper. I did not take part in any of the experiments.

## Paper II

As discussed earlier in this thesis, there is intense ongoing research to bring the operating temperature of THz QCLs up to room temperature, see Chap. 9 for details. In the second paper of this thesis, a new mechanism for the gain reduction in THz QCLs is presented, namely the temperature dependence of screening of ionized dopants by electrons in the laser. It is found that this is both the dominant and most temperature dependent scattering mechanism in the studied THz QCL. This mechanism is different from others since it acts independent of population inversion.

I performed the calculations, analyzed the data, and wrote a large part of the paper.

## Paper III

Acoustic phonon scattering strength is small compared to most scattering mechanism in QCLs. However, in Paper II, a phenomenological scattering strength was used, see App. B3 in Ref. [60]. Although small, acoustic phonon scattering constitutes the only coupling to the lattice temperature, and the only channel of inelastic scattering, at energies below the optical phonon energy. In the third paper of this thesis a microscopic form of the self-energy for interaction with a bath of acoustic phonon via the deformation potential interaction is derived.

The main achievement in this paper is that the effect of acoustic phonon scattering on the spectra is quantified.

I modified the code to include acoustic phonon scattering, performed the calculations and analyzed the data. I wrote a large part of the paper.

## Paper IV

In Paper IV, some of our work related to the optics of QCLs is summarized. More specifically, focused on the optical linewidth. The key point of my contribution to the paper is the comparison of different estimates for the width of the gain peak. A full NEGF gain calculation gives a linewidth in between the widths from a simple approach when neglecting correlation effects, and including them on the simplistic level, as presented in Paper V.

I performed the calculations, prepared Fig. 2, and participated in writing the paper.

## Paper V

When the screening related temperature dependent lasing performance degradation mechanism was proposed in Paper II, a very simple screening model was used. Also, one of the important approximations in the transport calculation is the so-called  $\mathbf{k}_{\text{typ}}$ -approximation, see App. B in Ref. [60]. In Paper V, different aspects of screened impurity scattering are studied in much more detail, via a numerical implementation to study impurity scattering alone.

There are two main findings in this paper. First, on the physics side, a more refined model, compared to the one used in Paper II, including the subband structure and temperature difference between the subbands, still shows a strong increase in impurity scattering with temperature due to less screening. Second, on the numerics side, the isotropic Debye screening model is an excellent approximation for THz devices at temperatures of interest.

I initiated the project, wrote the code, did all calculations, and wrote most of the manuscript.

I

Fingerprints of spatial charge  
transfer in quantum cascade  
lasers

Paper I



II

Temperature dependence of the  
gain profile for terahertz  
quantum cascade lasers

Paper II



# III

Temperature degradation of the  
gain transition in terahertz  
quantum cascade lasers – the role  
of acoustic phonon scattering

Paper III





# IV

## Simulation of gain in quantum cascade lasers

*Errata:*

Eq. 1 should read:

$$G_{\text{simple}}(\omega) = \frac{e^2 |z_{l_0, \text{up}}|^2 \omega (n_{\text{up}} - n_{l_0})}{2dc\epsilon_0 \sqrt{\epsilon_r}} \frac{\Gamma}{(E_{\text{up}} - E_{l_0} - \hbar\omega)^2 + \Gamma^2/4}$$

Paper IV



# V

## Temperature dependence and screening models in quantum cascade structures

*Errata:*

Below Eq. (11), should read:  $n_i = (2/A) \sum_{\mathbf{k}} f_{i,\mathbf{k}}$

Paper V

